

5-2019

Hypervelocity Impact Analysis of Hybrid Nanocomposite Sensors for Inflatable Space Structures

Yachna Gola

Follow this and additional works at: <https://commons.erau.edu/edt>



Part of the [Aerospace Engineering Commons](#)

Scholarly Commons Citation

Gola, Yachna, "Hypervelocity Impact Analysis of Hybrid Nanocomposite Sensors for Inflatable Space Structures" (2019). *Dissertations and Theses*. 461.

<https://commons.erau.edu/edt/461>

This Thesis - Open Access is brought to you for free and open access by Scholarly Commons. It has been accepted for inclusion in Dissertations and Theses by an authorized administrator of Scholarly Commons. For more information, please contact commons@erau.edu.

HYPERVELOCITY IMPACT ANALYSIS OF HYBRID NANOCOMPOSITE
SENSORS FOR INFLATABLE SPACE STRUCTURES

A Thesis

Submitted to the Faculty

of

Embry-Riddle Aeronautical University

by

Yachna Gola

In Partial Fulfillment of the

Requirements for the Degree

of

Master of Science in Aerospace Engineering

May 2019

Embry-Riddle Aeronautical University

Daytona Beach, Florida

HYPERVELOCITY IMPACT ANALYSIS OF HYBRID NANOCOMPOSITE
SENSORS FOR INFLATABLE SPACE STRUCTURES

by

Yachna Gola

A Thesis prepared under the direction of the candidate's committee chairman, Dr. Daewon Kim and Dr. Sirish Namilae, Department of Aerospace Engineering, and has been approved by the members of the thesis committee. It was submitted to the School of Graduate Studies and Research and was accepted in partial fulfillment of the requirements for the degree of Master of Science in Aerospace Engineering.

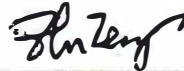
THESIS COMMITTEE



Chairman, Dr. Daewon Kim



Co-Chairman, Dr. Sirish Namilae



Member, Dr. Feng Zhu



Member, Dr. Virginie Rollin

x 

Graduate Program Coordinator, Dr. Magdy Attia

5-20-2019

Date



Dean of College of Engineering, Dr. Maj Mirmirani

5/20/2019

Date



Vice Chancellor of Academic Support, Dr. Christopher D. Grant

5/20/19

Date

ACKNOWLEDGMENTS

I would like to express my gratitude to my advisors and guides Dr. Daewon Kim and Dr. Sirish Namilae for their constant support and encouragement throughout this research. They always motivated me to push boundaries and accept challenges which helped my academic and professional growth. I am also grateful to them for helping me find financial aid which has contributed immensely towards completing my degree.

I am thankful to my thesis committee members, Dr. Feng Zhu and Dr. Virginie Rollin for their feedback, discussions and patience. I am thankful to the entire Aerospace Department at Embry Riddle, especially Mr. Mike Potash for helping me complete this research. I am thankful to my husband, Samaksh Behl for his moral support and positivity which kept me going every day. Lastly, I am immensely thankful to my parents, my family and my friends for their prayers and love.

TABLE OF CONTENTS

LIST OF TABLES	vi
LIST OF FIGURES	vii
ABBREVIATIONS	x
ABSTRACT.....	xi
1. Introduction	1
1.1. Motivation.....	3
1.2. Research Objectives	4
2. Background and Literature Review.....	5
2.1. Polymer Nanocomposites	5
2.2. Inflatable Space Habitats.....	8
2.3. Hypervelocity Impact by MMOD	10
3. Fabrication and Tensile Testing of Hybrid Nanocomposites.....	13
3.1. GNP Laser Cutting and Patterning	13
3.1.1. Development of Hybrid Nanocomposites.....	14
3.2. Tensile Testing of Patterned GNP-CNT Hybrid nanocomposites	16
3.3. Test Results	18
3.4. Discussion	21
4. Prototype Testing for Debris Detection	23
4.1. Test Setup.....	23
4.2. Single Sensor	24
4.3. Array of Sensors	26
4.4. Test Fixture Design and FEA for Hypervelocity Impact Test.....	27
4.5. Hypervelocity Impact Simulation: Baseline Model	27
4.6. Assumptions.....	28
4.7. Material Models.....	29
4.8. Results of the baseline model	31
4.9. Discussion	34
5. Hyper Velocity Impact Test	36
5.1. Hyper-Velocity Impact Test	36
5.1.1. Test Range.....	36
5.1.2. Test Articles and Test Setup	39
5.1.3. Projectile Description	41
5.1.4. Instrumentation	42
5.1.5. Velocity Measurement	43
5.1.6. Flash Radiography	45
5.2. Impact Test Results	45
5.3. First Impact Test	46
5.4. Resistance Measurement of Hybrid Sensors	52

5.5.	Second Impact Test	53
5.6.	Resistance Measurement of Hybrid Sensors	58
5.7.	Limitations of Hypervelocity Impact Test	59
5.8.	Discussion	60
6.	Conclusions and Future Work.....	64
6.1.	Conclusions.....	64
6.2.	Future Work.....	66
	REFERENCES	68
A.	APPENDIX	75

LIST OF TABLES

Table 4.1 Material Properties used in the simulation.	31
Table 5.1 Summary of the impact tests.....	46
Table 5.2 Comparison of sensitivity of capacitive sensors and hybrid nanocomposite sensors to impact damage at 7 km/s for a projectile of 3mm diameter.	62

LIST OF FIGURES

<i>Figure 2.1</i> (a) Single-walled carbon nanotube (b) Fullerenes (c) Graphene	6
<i>Figure 2.2</i> (Left) Typical Whipple shield (Right) Design for current study	12
<i>Figure 3.1</i> (a) CAD Model of laser mounted on the enclosure (b) Keyence Laser mounted on developed enclosure (c) Graphene sheet placed for cutting.	14
<i>Figure 3.2</i> 1 mm diameter circular GNPs obtained from laser cutting of graphite sheet. 14	
<i>Figure 3.3</i> (a) A pattern of GNP cut from Graphite sheet on top of Kapton® and 2216 translucent epoxy part-B (b) Graphite sheet peeled away from Kapton® (c) Pattern of GNP on Kapton® (d) CNT buckypaper with a layer of two-part 2216 translucent epoxy.	15
<i>Figure 3.4</i> CNP cuts by laser placed on top of Kapton®; (a) circular patterned GNP, (b) randomly placed circular GNP, (c) elliptical patterned GNP, and (d) randomly placed elliptical GNP.	17
<i>Figure 3.5</i> (a) CNT sheet with copper electrodes (b) Patterned elliptical GNP-CNT hybrid nanocomposite.....	18
<i>Figure 3.6</i> Effect of circular GNP alignment on the piezoresistivity of hybrid nanocomposites, from experimental results (average of 3 samples).	19
<i>Figure 3.7</i> Effect of patterned circular and elliptical GNP alignment on the piezo resistivity of hybrid nanocomposites, from experimental results (average of 3 samples).	20
<i>Figure 3.8</i> (Top) CNT+GNP epoxy nanocomposite specimen (bottom) CNT epoxy nanocomposite specimen.	20
<i>Figure 3.9</i> Effect of GNP on the piezo resistivity of the nanocomposites, from experimental results (average of 3 samples).	21
<i>Figure 4.1</i> Test Setup for prototype testing.	23
<i>Figure 4.2</i> Resistance change ratio by addition of 3 mm hole statically in 3 inch × 3 inch sensor.	25
<i>Figure 4.3</i> Resistance change ratio by addition of 4.5 mm hole statically in a 3 inch × 3 inch sensor.	25
<i>Figure 4.4</i> Circuit of four channel electronic control circuit.....	26
<i>Figure 4.5</i> Fixture Design.....	28
<i>Figure 4.6</i> Finite Element model of test article.	29
<i>Figure 4.7</i> Energy data from the baseline model.....	32
<i>Figure 4.8</i> Internal energy absorption by each layer	32
<i>Figure 4.9</i> Snapshot of hyper velocity impact simulation of baseline model	33
<i>Figure 4.10</i> Comparison of response of sensors to static and dynamic loading.....	34
<i>Figure 5.1</i> Test Range at UDRI hypervelocity impact laboratory (Courtesy of UDRI). .	37

<i>Figure 5.2</i> Gas gun chamber at UDRI, Impact Physics Laboratory, Range 4 (Courtesy of UDRI).	38
<i>Figure 5.3</i> Two-stage light gas gun firing cycle (Courtesy of UDRI).....	38
<i>Figure 5.4</i> Sabot and spherical projectile (Courtesy of UDRI).....	39
<i>Figure 5.5</i> Top view of the test article.....	40
<i>Figure 5.6</i> Various layers in the test article	41
<i>Figure 5.7</i> Test article Setup.....	42
<i>Figure 5.8</i> Circuit of nine channel electronic control circuit.....	43
<i>Figure 5.9</i> LabVIEW code for data acquisition of HVIT.....	44
<i>Figure 5.10</i> BNC feedthroughs and Swagelok fittings for instrumentation during the test.	44
<i>Figure 5.11</i> Test article before the impact.....	47
<i>Figure 5.12.</i> Test article after the impact.....	48
<i>Figure 5.13</i> Nomenclature used to recognize the hybrid sensors in an array.....	48
<i>Figure 5.14</i> Damage on the first layer (hybrid sensors) and the projectile after the first test	49
<i>Figure 5.15</i> Front side of the first layer (hybrid sensors) after first test.....	49
<i>Figure 5.16</i> Back side of the first layer (hybrid sensors) after first test	50
<i>Figure 5.17</i> Front side of the second layer (hybrid sensors) after first test	50
<i>Figure 5.18</i> Back side of the second layer (hybrid sensors) after first test	51
<i>Figure 5.19</i> Front side of the third layer (ink jet printed sensors) after the first test.....	51
<i>Figure 5.20</i> Back side of the third layer (ink jet printed sensors) after the first test	52
<i>Figure 5.21</i> Response of different sensors during first HVIT.....	53
<i>Figure 5.22</i> Test article before the test	54
<i>Figure 5.23</i> Test article after the test	55
<i>Figure 5.24</i> Front side of the first layer (inkjet-printed sensors) after the second test.....	55
<i>Figure 5.25</i> Back side of the first layer (inkjet-printed sensors) after the second test	56
<i>Figure 5.26</i> Front side of the second layer (inkjet-printed sensors) after the second test	56
<i>Figure 5.27</i> Back side of the second layer (inkjet-printed sensors) after the second test.	57
<i>Figure 5.28</i> Frontside of the third layer (ink jet printed sensors) after the second test	57
<i>Figure 5.29</i> Back side of the third layer (inkjet printed sensors) after the second test	58
<i>Figure 5.30</i> Response of different sensors during second HVIT.	59
<i>Figure A.1</i> Resistance change ratio for sensor 1 in the array during the first test.	75

<i>Figure A.2</i> Resistance change ratio for sensor 2 in the array during the first test	76
<i>Figure A.3</i> Resistance change ratio for sensor 3 in the array during the first test	76
<i>Figure A.4</i> Resistance change ratio for sensor 4 in the array during the first test	77
<i>Figure A.5</i> Resistance change ratio for sensor 5 in the array during the first test	77
<i>Figure A.6</i> Resistance change ratio for sensor 6 in the array during the first test	78
<i>Figure A.7</i> Resistance change ratio for sensor 7 in the array during the first test	78
<i>Figure A.8</i> Resistance change ratio for sensor 8 in the array during the first test	79
<i>Figure A.9</i> Resistance change ratio for sensor 9 in the array during the first test	79
<i>Figure A.10</i> Resistance change ratio for sensor 1 in the array during the second test	80
<i>Figure A.11</i> Resistance change ratio for sensor 2 in the array during the second test	80
<i>Figure A.12</i> Resistance change ratio for sensor 3 in the array during the second test	81
<i>Figure A.13</i> Resistance change ratio for sensor 4 in the array during the second test	81
<i>Figure A.14</i> Resistance change ratio for sensor 5 in the array during the second test	82
<i>Figure A.15</i> Resistance change ratio for sensor 6 in the array during the second test	82
<i>Figure A.16</i> Resistance change ratio for sensor 7 in the array during the second test	83
<i>Figure A.17</i> Resistance change ratio for sensor 8 in the array during the second test	83
<i>Figure A.18</i> Resistance change ratio for sensor 9 in the array during the second test	84

ABBREVIATIONS

CNT	Carbon Nanotubes
DAQ	Data Acquisition
GNP	Graphene Nano Platelets
HVIT	Hyper Velocity Impact Test
MMOD	Micrometeoroid
PNC	Polymer Nanocomposites
UDRI	University of Dayton Research Institute

ABSTRACT

Future space exploration requires easy-to-transport, and easy-to-build and deploy space habitats. NASA and Bigelow Aerospace have collaborated so that human habitation can be made safe and easy with inflatable space habitats (Litteken, 2017). One of the biggest threats faced by these structures in outer space is impact damage by micrometeoroid orbital debris (MMOD) traveling at velocities as high as 15 km/s (Lemmens, Krag, Rosebrock, & Carnelli, 2013). This work presents fabrication and testing of hybrid nanocomposites with carbon nanotubes (CNT) and coarse graphene nanoplatelets (GNP) as fillers and flexible epoxy matrix, that are proposed to be used for sensing the impact damage by MMOD in space inflatable structures. CNT and GNP were chosen as fillers owing to their excellent electrical properties and piezoresistivity. A new method was developed to cut graphite sheet (composed of GNPs) in laser marker and distribute it in patterns on carbon nanotube sheet (buckypaper) in epoxy matrix. Piezoresistivity tests were carried out and results were compared with percolation-based Monte Carlo simulations from past research. A hypervelocity impact test was designed and executed at the University of Dayton Research Institute, Ohio, to test the response of the sensors to hypervelocity impacts. Aluminum spheres of 3 mm diameter and 4.5 mm diameter were accelerated to 7 km/s and shot at the sensors, and results were recorded during and after the test. A periodic scanning multichannel control circuit was designed to power the sensors. LabVIEW codes were used for data acquisition and recognizing the location of the damage. The results proved that the hybrid CNT-GNP/epoxy nanocomposites can be used to create a damage detection system which would not only detect the impact damage caused by MMOD of 3mm diameter traveling at 7km/s but also discern its location and

depth of penetration by the MMOD.

1. Introduction

Hybrid composites refer to composites with either multiple filler/fiber materials or multiple matrix materials. This work discusses hybrid nanocomposites made of two particulate fillers; carbon nanotubes and graphene platelets, in an epoxy matrix.

Carbon nanotubes are known to have supreme mechanical and electrical properties and are a popular choice for fillers in polymer nanocomposites (Bhattacharya, 2016; Moniruzzaman & Winey, 2006; Fiedler, Gojny, Wichmann, Nolte, & Schulte, 2006).

On the other hand, recent studies have shown that individual graphene sheets have extraordinary electronic transport properties, and one possible route to harnessing these properties for applications is to incorporate graphene sheets in a composite material (Stankovich, et al., 2006; Ramanathan, et al., 2008). Despite the numerous studies focused on the use of CNTs or GNPs as fillers to improve the electrical conductivity and electromechanical behaviors of polymer composites, relatively few studies have examined hybrid CNT–GNP composites (Gbaguidi, Namilae, & Kim, 2017; Lee, Jug, & Meng, 2013; Hwang, Park, & Park, 2013; Luo & Liu, 2013).

CNT based nanocomposites are known to exhibit a change in electrical resistance when loaded mechanically. This phenomenon is called piezoresistivity. Although CNT-based nanocomposites have been reported to show excellent piezoresistive properties (Obitayo & Liu, 2012; Hu, Fukunaga, Atobe, Liu, & Li, 2011; Dharap, Li, Nagarajaiah, & Barrera, 2004), addition of a second filler like graphite nanoplatelets (GNP) was found to further enhance their performance (Namilae, Li, & Chava, 2018). An explanation for this improvement is the bridging of CNT network by planar graphitic platelets resulting

in a continuous network of fillers. Owing to their piezoresistivity, their mechanical and electrical response is coupled and they can be used for various strain sensing applications.

Health monitoring and damage detection are challenging when it comes to space inflatable structures as traditional methods with strain gage and fiber optic sensors cannot be employed. These methods are more suitable for rigid structures, where mounting of sensors, power distribution, and data communication are not an issue. In the case of inflatable structures, the sensors need to be pre-positioned before packing and need to maintain integrity while folding and deployment. If the sensors are mounted after deployment, there is no way to monitor the health of the structure before deployment. Issues related to cabling also become manifold when it comes to inflatable structures (Kennedy, Raboin, Spexarth, & Valle, 2000). The impact detection system would need to locate the damage, its size and depth of penetration in real time and warn the crew so that immediate action can be taken. To meet all these requirements one approach is to execute a flexible blanket of sensors that can detect impact and are integrated with the soft layers of inflatable structure in critical areas.

One of the technologies designed for inflatable habitat materials is based on embedded capacitors (Brandon, et al., 2011). An array of capacitors made of flexible circuit technology act as impact damage sensors. Any penetration due to the damage is manifested as a change in applied voltage due to change in the area of the dielectric layer. Another type of sensors is passive wireless sensor tags that operate via radio-frequency energy transmitted from an interrogation device (Brandon, et al., 2011). They can provide information on other physical parameters like temperature, humidity, acceleration, etc. In this report, hybrid GNP-CNT/epoxy nanocomposites, owing to their piezoresistivity,

flexible matrix, mechanical strength and light weight will be explored for their feasibility to be integrated with walls of the inflatable structures.

1.1. Motivation

This work is done as a part of NASA SBIR Phase II of “Integrated Structural Health Sensors for Inflatable Space Habitats”. Phase I was completed successfully with experimental proofs showing that CNT-GNP hybrid nanocomposites have strain, vibration and damage sensing capabilities (Anees M., 2017). It was also proven that piezoresistivity is higher for 5 wt. % of GNP and CNT in epoxy (Li & Namilae, 2016). Additionally, it was found that using a flexible matrix of two-part 3M Scotch-Weld translucent epoxy adhesive 2216 gave up to 11% strains, and more than 5 times better piezoresistive response than the other CNT/epoxy based composites (Anees M., 2017). However, the techniques employed to develop these hybrid composites involved cutting GNP by hand and infiltrating the CNT with evenly mixed epoxy-GNP of specified weight percent, which did not offer reproducibility and could not be numerically modeled to validate or predict the response.

In the following sections, a novel technique to fabricate hybrid nanocomposites with uniformly distributed GNP along with CNT is proposed, and their strain dependent electrical resistivity is studied. Finally, based on results from testing and numerical simulations, a comparative analysis of the effect of patterning on the piezoresistive response of the composites is done. The final step towards confirming the feasibility of using the hybrid nanocomposites for sensing applications in space is to test the sensors for their response to impact damage by projectiles traveling at hyper velocities. Integrating the sensors to develop a complete damage detection and monitoring system

would also require an efficient power system to scan the sensors every cycle, and a warning system to give information on damage. These areas have motivated the research presented here.

1.2. Research Objectives

The main research objective is to showcase the ability of these sensors to detect damage caused by MMOD impact, location of damage within an array of sensors (planar) as well as the depth of penetration by the projectile. To reach this goal, the following milestones were set and achieved:

- 1) Devise a method to cut graphene nanoplatelets such that shape and size can be controlled, and the process is time efficient.
- 2) Distribute the GNP in desired patterns on nanocomposites to study the effect of aspect ratio and distribution of GNP on the piezoresistive performance of the sensors and compare it with numerical results.
- 3) Design test article and test fixtures for the hypervelocity impact testing of an array of hybrid nanocomposite sensors. This entails sizing analysis of the sensors and creating a test article that would simulate the layers of space inflatable structures
- 4) Design and test a circuit to perform periodic scanning of the sensors that can be used during the test as well as used as a base model for further research on the power system.
- 5) Design a data acquisition system using LabVIEW to get real-time data during the test.
- 6) Plan and execute a hypervelocity impact test to study the performance of the sensors when hit by a projectile of 3mm diameter traveling at 7 km/s.

2. Background and Literature Review

2.1. Polymer Nanocomposites

Nanocomposites were revolutionized when Toyota researchers revealed that adding Mica to Nylon resulted in a fivefold increase in material's yield and tensile strength (Balazs, Emrick, & Russell, 2006). Since then researchers have explored and pondered polymer and nanoparticle composites that are now widely used in the aerospace industry. Polymer nanocomposites (PNC) are fabricated by depositing very small particles, typically having a diameter less than 100 nm, in a host polymer matrix (Njuguna & Pielichowski, 2003). Traditionally polymer composites consist of a large volume (> 60 vol %) of fillers in the matrix (Keller, 2011), however nanocomposites consist of very low (< 2 vol %) volume of nanofillers like nanoclays (Ray & Okamoto, 2003; Usuki, Hasegawa, & Kato, 2005), graphite nanoplatelets (Zheng & Wong, 2003; Zheng, Lu, & Wong, 2004; Cho, Lee, Yang, Fukushima, & Drzal, 2005; Ramanathan, 2007), and carbon nanotubes (Ajayan, Schadler, Giannaris, & Rubio, 2000; Thostenson, Ren, & Chou, 2001; Ramanathan, Liu, & Brinson, 2005) that result in a vast change in properties of the composite. Mechanical properties such as tensile strength, toughness, elasticity and other properties like thermal and electrical conductivity of PNCs are improved depending on the properties of the nanofillers. Even a low volume fraction of well-dispersed nanofillers creates a large interfacial area resulting in a continuous network of altered polymer chains in the matrix that alters its properties fundamentally (Ramanathan, et al., 2008). This is due to the large surface area per unit volume they provide. For electronic applications, based on the requirement, enough conductivity is added in the matrix to provide electronic discharge, by using conductive fillers. The

fillers form a three-dimensional network through the component due to which high conductivity is achieved. This phenomenon is called percolation. Percolation theories are often used to describe conductive properties of composites made of conductive fillers and matrix. The percolation threshold is a measure of the conductivity of these composites and has been proven to be highly dependent on the aspect ratio of the filler particles. This work discusses PNCs developed with carbon nanotubes and graphene nanoplatelet fillers in epoxy matrix, which results in nanocomposites that have intrinsic electromechanical properties.

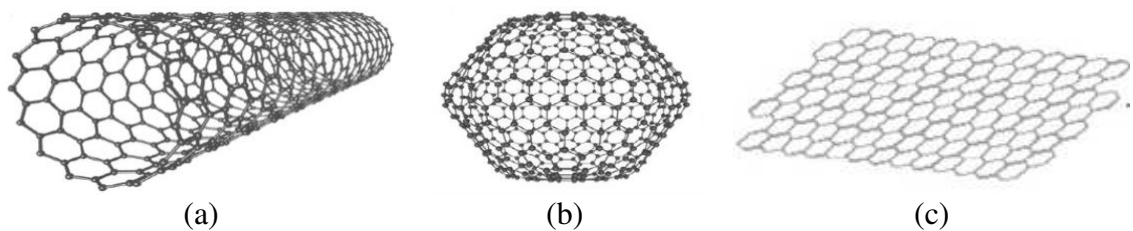


Figure 2.1 (a) Single-walled carbon nanotube (b) Fullerenes (c) Graphene

Carbonaceous nanofillers include carbon nanofibers, carbon nanotubes and emerging graphene nanoplatelets. Carbon nanotubes (CNT) are long slender fullerenes, where the walls of the tubes are hexagonal carbon or graphite structure, as shown in Figure 2.1 (a). Fullerenes are cage-like structures of carbon atoms which are made of hexagonal and pentagonal faces (Figure 2.1 (b)). CNTs are strong (Li, et al., 2005) and their extremely small size makes it ideal to be embedded in various types of materials as reinforcements to form lightweight strong nanocomposites. They have remarkable mechanical properties, high electrical and thermal conductivity and high aspect ratios. Since percolation thresholds depend on aspect ratio, carbon nanotubes have proven to be an excellent choice as fillers in polymer composites (Sandler, Kirk, Kinloch, Shaffer, & Windle, 2003). The electrical conductivity of CNT/epoxy nanocomposites can be enhanced by several orders

just by adding 0.5 wt. % of CNTs (Ma, Siddiqui, Marom, & Kim, 2010).

Graphene is considered a two-dimensional carbon nanofiller with one atom thick planar sheet of sp² bonded carbon atoms that are densely packed in a honeycomb crystal lattice (Figure 2.1 (c)). Graphene is preferred as a nanofiller over many other nanofillers due to its intrinsic properties. It has excellent electronic properties, since electrons move through its planar structure without much scattering or resistance. It has been predicted that a defect-free graphene platelet could have intrinsic tensile strength higher than any other material and can withstand ultra-high strains (Zhao, Nardelli, & Bernholc, 2002). Graphene exhibits thermal conductivity several times higher than Copper (Mukhopadhyay & Gupta, 2011). In addition, it has a high aspect ratio making it an impressive choice as nanofillers in nanocomposites (Kuilla, et al., 2010). When compared to other fillers like nanosized steel, natural rubber, Kevlar fiber, HDPE plastics and CNT, Graphene has the highest tensile strength of 130 GPa, highest thermal conductivity of 5.3×10^3 W/mk at room temperature and electrical conductivity of 7200 S/m which is 1.8 times that of CNTs (Kuilla, et al., 2010). Graphene-based nanocomposites are used in anti-static coatings, sensors, batteries, solar cells and transparent conductors (Al-Saleh, 2015).

Enhancement of properties in polymer nanocomposites has been explored by mixing two different fillers while maintaining the total amount, to form ternary hybrid nanocomposites (Sagalianov, Vovchenko, Matzui, & Lazarenko, 2017). The reason for this effect in CNT-GNP/epoxy composites in context with their improved electrical properties is that CNTs form a bridge between GNPs resulting in a continuous conductive network. The electrical conductivity of CNT-GNP/epoxy hybrid nanocomposites is found

to be many times more than nanocomposites with CNT alone and nanocomposites with GNP alone (Li, Wong, & Kim, 2008).

Besides the exceptional mechanical, thermal and electrical properties of CNTs, one of their other lucrative properties is their self-sensing nature due to the coupling of mechanical deformation and electrical properties (Li, Dichiara, & Bai, 2013). As mechanical strain is applied, the microstructure or the conductive network of CNTs changes, giving rise to a change in resistance. This property is called piezoresistivity. CNT-based polymer composites can thus be used for strain sensing applications. Several works discuss the development of piezoresistive sensors with CNT polymer nanocomposites (Dharap, Li, Nagarajaiah, & Barrera, 2004; Kang, Schulz, Kim, Shanov, & Shi, 2006). The sensitivity of piezoresistive sensors is measured by the gage factor, which is defined as the fractional change in resistance per unit strain. GNP based polymer nanocomposites also show piezoresistive properties. The reason for their intrinsic piezoresistive behavior is the same as for CNT based PNCs. A number of experimental and numerical works have been done on the piezoresistivity of GNP based nanocomposites (Bae, et al., 2013; Bonavolontà, et al., 2016; Das & Prusty, 2013). Adding GNP as the second filler to CNT/epoxy PNCs has shown to improve their piezoresistive response (Hwang, Park, & Park, 2013; Park, Kim, Park, & Shim, 2011; Luo & Liu, 2013). The focus of this work is to exploit the self-sensing properties of CNT-GNP/epoxy hybrid nanocomposites to develop flexible lightweight strain sensors.

2.2. Inflatable Space Habitats

Inflatable space habitats can be defined as pressurized structures that can support human life in outer space. They typically consist of several soft foldable constituent

layers like inner liner, bladder, restraint layer, thermal control layer and protective layers (Brandon, et al., 2011). In 2006, Genesis I became the first space module to be successfully sent into orbit by Bigelow Aerospace, testing various systems, materials, and techniques related to determining the viability of long-term inflatable space structures (Genesis I, 2019). Following that, in 2007, Genesis II, the second module was sent into orbit by the company, to build on the data and experience gleaned from its previously orbited sister-ship Genesis I (Genesis II, 2018). In 2016, The Bigelow Expandable Activity Module (BEAM), an experimental expandable capsule, docked with the International Space Station (ISS) (Advanced Exploration Systems, 2017). Inflatable structures are becoming one of the top choices to make human habitation possible in space due to large operational volume as compared to smaller launch volumes. This can be achieved by various efficient packing concepts. The materials used should have less weight, high tensile strength, good flexibility, durability and resistance to harsh space environments. (Häuplik-Meusburger, Sommer, & Aguzzi, 2009). Besides using an appropriate material with the right properties, it is also imperative that the habitats can withstand damage caused by Micrometeoroid and Orbital Debris (MMOD). As of January 2019, the number of space debris of size 1 mm to 1 cm in Earth orbit was estimated around 128 million with impact velocities that can reach 15 km/s (Lemmens, Krag, Rosebrock, & Carnelli, 2013). Damage caused by these ranges from small pits/hole penetrations to mission-critical damage for larger than one-centimeter projectiles. To protect space structures from MMOD impacts, passive protection can be achieved by having outer skin consist of multiple protection layers. Detection of impact damage and its location would help in mission success for manned and unmanned space crafts.

Damage detection and its location can provide valuable time to implement repairs or isolation of leaking areas of the habitat. For reentry vehicles, information about damage detection and its location could give time for repairs, replacements, and change of trajectories to limit the heating.

2.3. Hypervelocity Impact by MMOD

As of January 2019, 34 000 objects more than 10 cm, 900 000 objects from 1 cm to 10 cm and 128 million objects from 1mm to 1cm were estimated by statistical models to be in low earth orbit (Space Debris, 2018). Small objects can cause mission critical damage at hyper velocities. Large objects can be avoided through active measures and maneuvers, but small objects can only be avoided by passive methods like MMOD shields that form a part of the spacecraft or space habitat. Effect of hypervelocity impact depends on projectile and target material, impact velocity, incident angle and shape of projectile. Hypervelocity Impact test is the most important step in validating the design of MMOD shielding (Space Debris, 2018). During these tests, two or three stage light gas guns are used to accelerate projectiles to hyper velocities. The guns can launch a variety of projectile shapes in a controlled environment.

Typical MMOD shields have Whipple shield type of design. The main components are bumper and rear wall. The purpose of the bumper is to break the projectile into a cloud of material containing projectile and bumper debris. This cloud expands while it moves towards the rear wall and momentum and energy are distributed over the area. The rear wall faces a blast loading from the debris cloud. Variations of Whipple shield include stuffed Whipple and flexible multi-shock Whipple shields (Christiansen, Nagy, Lear, & Prior, 2009). The efficiency of MMOD shields depends on

the state of debris cloud created when the bumper is hit by the projectile. The debris cloud can consist of solid, liquid and/or vaporized material depending on the interaction between projectile and bumper at the impact, which is directly related to mechanical and thermal properties of materials, and impact pressure generated. Higher impact pressure results in fewer solid fragments and more vapor content. Impact pressure depends on projectile velocity, angle of incidence and density of projectile and bumper. Initially, a compressive wave is generated at the impact, which results in an increase in density and temperature of projectile and bumper. Compressive waves are also generated that travel through the materials at free surfaces. If stress near the free surfaces exceeds the tensile strength of the materials, debris is created. Temperature rises during this process due to the increase in internal energies, which can melt and vaporize the materials (Arnold, et al., 2009).

Stuffed Whipple shield includes Nextel ceramic fabric and high strength Kevlar fabric between the bumper and rear wall (Christiansen, Nagy, Lear, & Prior, 2009). This arrangement provides better protection from MMOD as the momentum of the debris cloud is decreased by the extra layers even more before it hits the rear wall. While the ceramic fiber layer breaks the debris fragments, the high strength fiber layer slows the expansion of the cloud without contributing to the material in the cloud. Multi shock shields comprise of multiple bumpers made of ceramic fabric and a Kevlar or aluminum rear wall. Figure 2.2 shows the design of a typical Whipple shield and the multi-shock type of design.

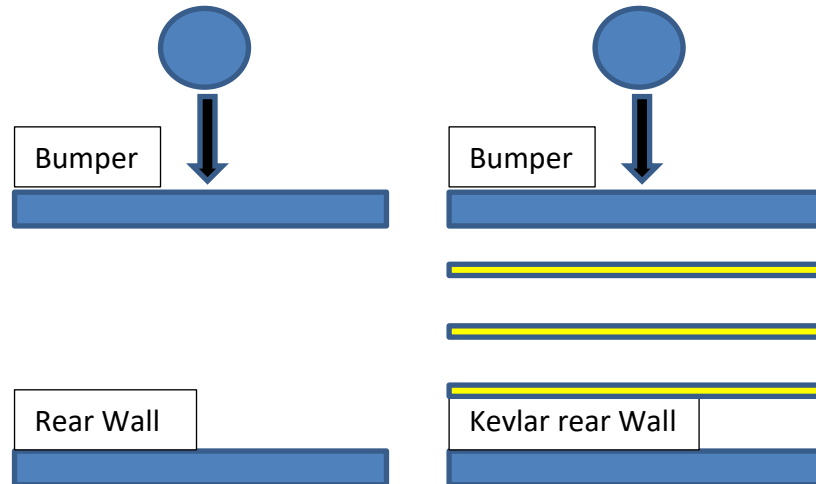


Figure 2.2 (Left) Typical Whipple shield (Right) Design for current study

Ceramic layers break up the projectile more efficiently due to higher shock pressures. Besides, they do not produce much secondary debris (Arnold, et al., 2009).

Multi-shock shield design is used for MMOD shields in space inflatable habitats. The test article and fixtures for the hypervelocity test were designed keeping in mind this arrangement of the MMOD shield.

3. Fabrication and Tensile Testing of Hybrid Nanocomposites

3.1. GNP Laser Cutting and Patterning

In this section, development of the laser cutting process of the graphite sheet to form nanoplatelets, which are used as second fillers in the composite, and GNP patterning on CNT buckypaper is discussed. In the development of nanocomposites, GNP was previously obtained by cutting graphene sheet using a knife blade. This process was time-consuming and did not give uniform sized platelets. Therefore, an automated process for laser cutting was developed. An MD-X 1520 laser marker by Keyence was selected for this purpose. Figure 3.1(a) shows the CAD Model of the laser marker mounted on the enclosure. Figure 3.1(b) shows the actual laser and developed enclosure. Figure 3.1(c) shows a graphite sheet placed on a variable height stand for cutting. Furthermore, it was observed that even though the platelets were uniformly cut, their distribution was random on CNT which made it difficult to predict and relate the results with the numerical model. Based on these considerations and the following advantages, laser cutting and GNP patterning on CNT were found to be imperative:

- 1) Easy control on size and shape of GNPs.
- 2) Automated cutting process in an enclosed area makes the working environment safer.
- 3) Increase time efficiency.
- 4) Can be used to find the relation between macro and microstructure studies (compare to simulations).
- 5) Useful for optimization of shape and size for the highest piezoresistive response.



Figure 3.1 (a) CAD Model of laser mounted on the enclosure (b) Keyence Laser mounted on developed enclosure (c) Graphene sheet placed for cutting.

3.1.1. Development of Hybrid Nanocomposites

A uniform pattern of GNP can be easily cut from the graphite sheet using laser (Figure 3.2), but a technique had to be employed to carry the pattern to CNT buckypaper without moving the platelets. Kapton® was chosen as a substrate to transfer the platelets on to the buckypaper. Graphite sheet was cut on top of Kapton® in the laser and the Kapton®, carrying this pattern, was turned over on top of the buckypaper. The following section explains the experimental procedure in detail.

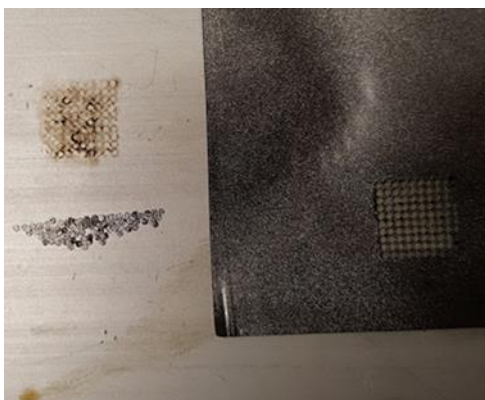


Figure 3.2 1 mm diameter circular GNPs obtained from laser cutting of graphite sheet.

The composites were made using CNT buckypaper and graphite platelets in a matrix of two-part 3M Scotch-Weld translucent epoxy adhesive 2216. A multiwall

carbon nanotube buckypaper consisting of 100% free-standing nanotubes, with an area density of 21.7 g/m² and surface electrical resistivity of 1.5 Ω /m² was obtained from nanotech Labs. The platelets were cut from a graphene sheet with surface resistivity of 2.8x10⁻² Ω /m², acquired from Graphene Supermarket. To fabricate the composites, the CNT sheet was first cut into 63.5 mm x 38.1 mm (2.5 inch x 1.5 inch) strip samples. 32-gauge copper electrodes were attached to both ends of the CNT sheet using conductive silver epoxy adhesive. The graphene sheet was cut into graphite nanoplatelets of the desired shape, using the Keyence MD-X-1000/1500 series 3 axis laser marker. A thin layer of the epoxy was applied between the Kapton® and graphene sheet, which ensured that the platelets would not displace while moving them to the CNT. Previously, this step was carried out with epoxy part B only, which led to uncured epoxy resin.

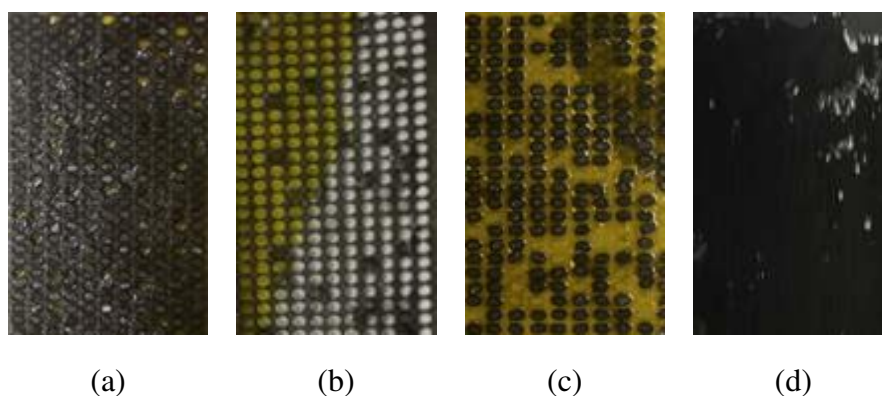


Figure 3.3 (a) A pattern of GNP cut from Graphite sheet on top of Kapton® and 2216 translucent epoxy part-B (b) Graphite sheet peeled away from Kapton® (c) Pattern of GNP on Kapton® (d) CNT buckypaper with a layer of two-part 2216 translucent epoxy.

To achieve a pattern of GNP, the laser was set to cut repeated rows and columns of the circles or ellipses. The graphene sheet was carefully peeled away leaving GNP on the Kapton®. Marking laser properties such as power, scan speed, and frequency, were set so that laser would cut the graphene sheet while not damaging the Kapton® beneath it. The cut GNP platelets were then transferred to the CNT sheet, which already carried

the matrix. Alignment of the platelets was kept such that major axes of the ellipses were parallel to the electric fields. Five (5) wt. % of the platelets were used with the epoxy in each sample. For achieving a random distribution, the platelets were displaced around on the Kapton® before moving them to the CNT sheet. The composites were vacuum bagged and cured for one hour at 200 degrees Fahrenheit. Each specimen was further cut into three specimens measuring 63.5mm x 12.7 mm (2.5 inch x 0.5 inch).

There were a few observations made while following this method. Firstly, the adhesive applied between Kapton® and graphene while cutting the pattern, not only shielded the Kapton®, but made the transfer much easier as the platelets would not move, and graphene sheet could be easily peeled away. Secondly, buckypaper had to be infiltrated by epoxy before flipping the Kapton® on the CNT buckypaper, as the application of epoxy without moving the platelets would be impossible. Since it could not be ensured that the Kapton® was not damaged by the laser, a layer of Kapton® tape was put on top of the nanocomposite. Lastly, a limitation of this method of developing the sensors was that 100% of GNP could not be transferred to the buckypaper (Figure 3.3). This could be due to the uneven surface of the graphene sheet, which was not marked efficiently in thicker regions.

3.2. Tensile Testing of Patterned GNP-CNT Hybrid nanocomposites

The procedure of patterning GNP on CNT buckypaper was used to study the effect of size and orientation of the graphite platelets on the piezoresistive response of the hybrid nanocomposites. Four different types of specimen were fabricated for a comparative analysis; buckypaper with patterned circular GNP of radius of 1 mm (Figure 3.4 (a)), buckypaper with randomly placed circular GNP of radius of 1 mm (Figure 3.4

(b)), buckypaper with patterned elliptical GNP of major axis 3 mm and minor axis 1 mm (Figure 3.4 (c)) and buckypaper with randomly placed elliptical GNP of major axis 3 mm and minor axis 1 mm (Figure 3.4 (d)). Content of GNP was kept constant in all the samples.

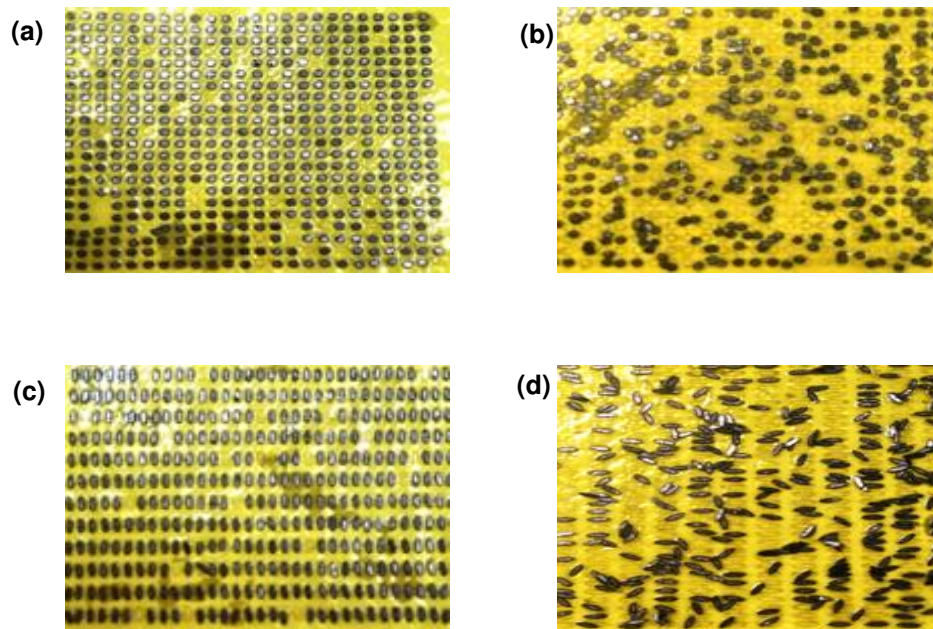


Figure 3.4 CNP cuts by laser placed on top of Kapton®; (a) circular patterned GNP, (b) randomly placed circular GNP, (c) elliptical patterned GNP, and (d) randomly placed elliptical GNP.

A four-point probe measurement was used to measure the change in voltage and consequently the change in resistance while applying mechanical loading on the specimen. A LABVIEW code was used along with a DAQ system to record the change in voltage, while the tensile test was conducted at a constant speed of 10mm/minute in a digital force tester. A constant intensity current of 0.103 amperes was passed through the specimen. Figure 3.5 shows the buckypaper with copper electrodes and the final hybrid nanocomposite with elliptical graphite platelets.

3.3. Test Results

Tensile tests were carried out to study the response of shape and spatial arrangement of GNP on the piezoresistive response of the sensors. The tensile testing of circular patterned and randomly placed GNP-CNT nanocomposites yielded the results shown in Figure 3.6. Average of three test specimens showed that resistance changed non-linearly with strain as in the case of elliptical GNP. Furthermore, patterned circular GNP and randomly placed GNP exhibited the same piezoresistive response.



Figure 3.5 (a) CNT sheet with copper electrodes (b) Patterned elliptical GNP-CNT hybrid nanocomposite

Specimens with a random distribution of GNP were prepared by cutting the graphene sheet in laser in a pattern and then moving the platelets. Therefore, this distribution cannot be called truly random. To see if this effect was contributing to the behavior of the nanocomposites as described in the previous section, patterned circular GNP-CNT and patterned elliptical GNP-CNT hybrid composites were tested and compared. The results are depicted in Figure 3.7, where the average of three samples showed non-linear resistance change with strain and no difference in the piezoresistive responses.

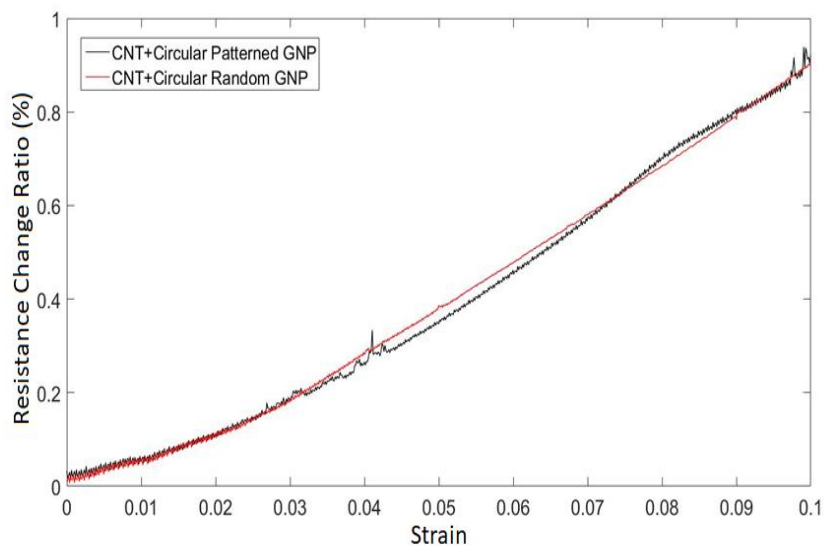


Figure 3.6 Effect of circular GNP alignment on the piezoresistivity of hybrid nanocomposites, from experimental results (average of 3 samples).

Another possible reason for no effect of shape or spatial arrangement/ patterning of GNP on the piezoresistive response of the composite could be the novel way of developing the sensors, which hindered the interaction between GNP and CNT. To establish the reliability of the sensor development method and testing procedures, tensile testing was done on CNT epoxy and CNT-GNP epoxy hybrid nanocomposites, which had been tested before and proved the fact that adding GNP to the nanocomposites enhances their piezoresistive response.

Following the same method, two types of specimens were prepared; CNT/epoxy nanohybrid composite with Kapton® on top and CNT-GNP/epoxy nanohybrid composite with Kapton® on top. Sample dimensions and test settings were the same as in previous tensile tests. GNPs were distributed on CNT in a random fashion as shown in Figure 3.8. Figure 3.9 shows the results of the tensile testing.

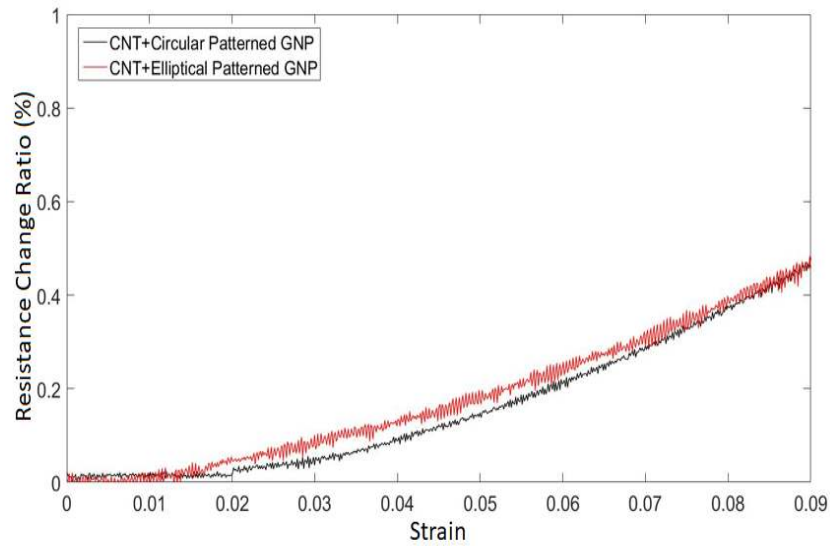


Figure 3.7 Effect of patterned circular and elliptical GNP alignment on the piezo resistivity of hybrid nanocomposites, from experimental results (average of 3 samples).

As expected, the piezoresistive response of the composite with GNP infiltrated epoxy was higher than that of CNT epoxy composite. This proved that interaction between GNP and CNT was intact and the technique followed to make the sensors with patterned GNP gave reliable results. Based on the discussion above, it can be concluded that patterning/ spatial arrangement and shape of GNP do not have any effect on the piezoresistive response of the CNT-GNP hybrid nanocomposites. However, results from the numerical model suggest that uniform distribution of GNPs and their aspect ratio increase the piezoresistive performance of the composites (Gbaguidi, Namilae, & Kim, 2017).

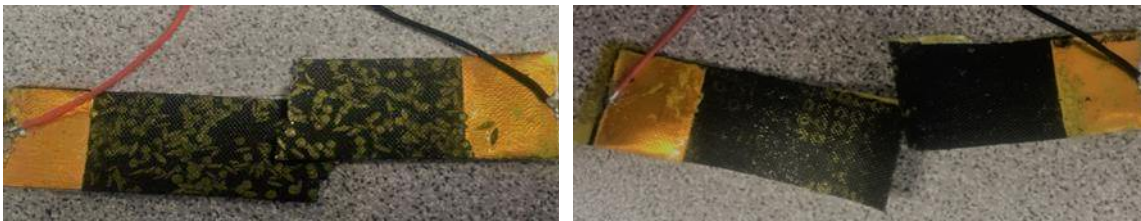


Figure 3.8 (Top) CNT+GNP epoxy nanocomposite specimen (bottom) CNT epoxy nanocomposite specimen.

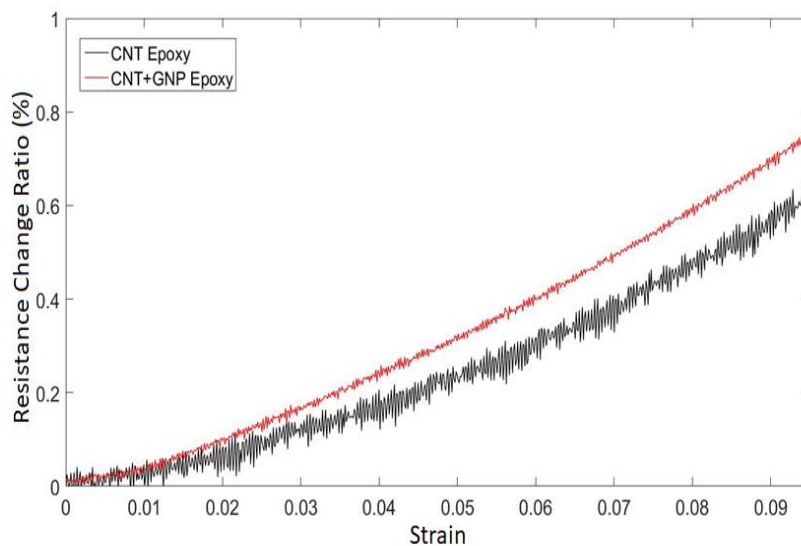


Figure 3.9 Effect of GNP on the piezo resistivity of the nanocomposites, from experimental results (average of 3 samples).

3.4. Discussion

Two phenomena were studied; effect of the aspect ratio of GNP, and effect of the distribution of GNP on piezoresistivity and electrical conductivity of the nanocomposites. Tensile tests were carried out to draw a comparison between piezoresistivity of circular and elliptical GNP-CNT nanocomposites and between patterned and randomly distributed GNP-CNT nanocomposites. The results showed that the aspect ratio and patterned/uniform distribution of GNP did not have any effect on the piezoresistive response of the sensors. Gbaguidi et al., 2017 presents a microstructure numerical model of CNT-GNP/epoxy hybrid nanocomposites which is used to show that piezoresistivity and electrical conductivity increase with GNP aspect ratio and their uniform alignment in the nanocomposites. CNT-GNP hybrid nanocomposites have shown improvement in mechanical, electrical and thermal properties when different aspect ratios and size of fillers are used (Chatterjee, et al., 2012) (Yue, Pircheraghi, Monemian, & Manas-

Zloczower, 2014) (Yu, et al., 2008). One of the possible explanations for the results achieved with experimentation presented here could be that the GNP fillers were macro level, whereas, the numerical models and experimentation done in past have been done on micro level.

4. Prototype Testing for Debris Detection

This chapter entails details about the preliminary tests conducted with prototypes of the sensor, data acquisition system and electronic circuit design and fabrication. This study also presents a preliminary finite element model of the hypervelocity impact test. Size of the sensors, required power and required sampling rates in the hypervelocity impact test discussed in Chapter 5, are chosen based on the results from the tests presented here. Fixture design and test article are discussed to show their similarity with soft layers of space inflatable structures.

4.1. Test Setup

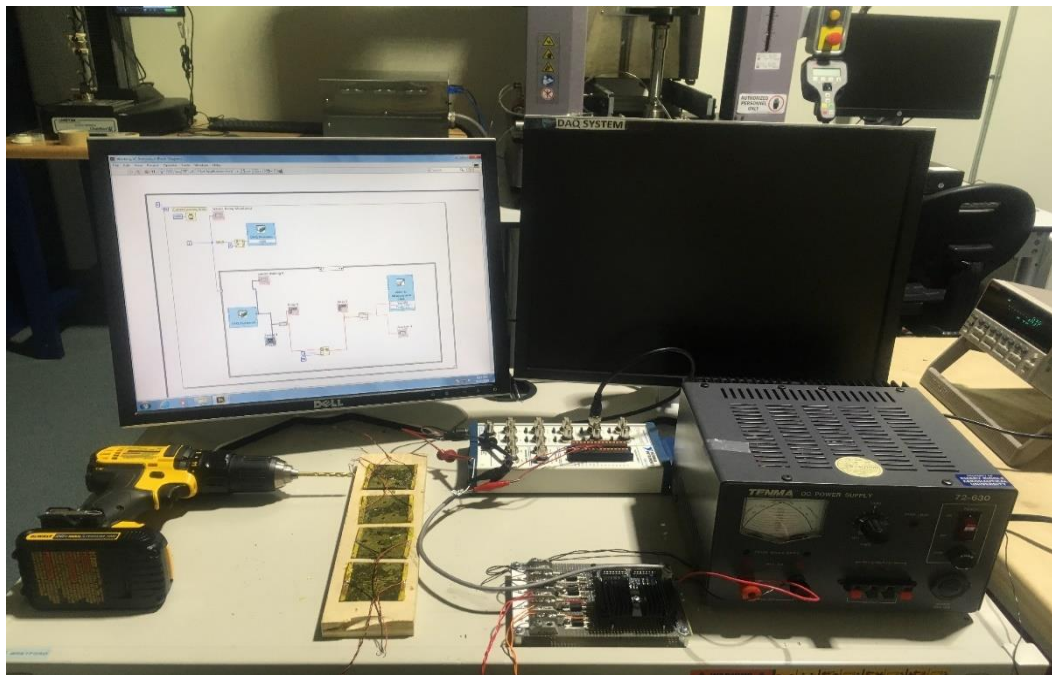


Figure 4.1 Test Setup for prototype testing.

The main objective of this test was to study the response of sensors to holes measuring at least 3mm diameter and verifying the capability of the data acquisition system to capture the change in voltage. The change in electrical resistance by drilling 3 mm holes was recorded in 2 inch \times 2 inch nanocomposites. Two configurations (single

sensor and arrays of sensors) of sensors were tested for change in electrical resistance as holes were added successively. Two different types of circuits were designed for the two configurations to send 0.5 A current. For single sensor testing, the circuit sent continuous current, whereas for an array of sensors, the circuit sent current periodically. A hand drill was used to simulate damage of 3 mm and 4.5 mm to the sensors. The change in voltage was recorded using LabVIEW codes, as damage was simulated in the sensors. The voltage readings were then converted to percentage change in resistance ratio (change in resistance over original resistance). Reliability of the LabVIEW codes and data acquisition system were tested by comparing the results with voltage readings from a multimeter before and after addition of holes. Figure 4.1 shows the test set-up for prototype testing.

4.2. Single Sensor

Samples were tested for two hole/damage sizes; 3 mm and 4.5 mm. Various intensities of current were passed through the samples and change in resistance due to self-heating was recorded. A high value of current would result in a measurable change in resistance, but also caused higher self-heating. It was observed that 0.5 A current caused low ohmic heating and gave measurable results. The circuit designed for this experiment sent 0.5 A current continuously to the sensor. Voltage readings were recorded by the DAQ after addition of each hole in both the specimens. The results were plotted (Figure 4.2 and Figure 4.3) and it was seen that the changes in resistance were detectable and measurable. It was observed that the change in resistance after the addition of each hole was stable.

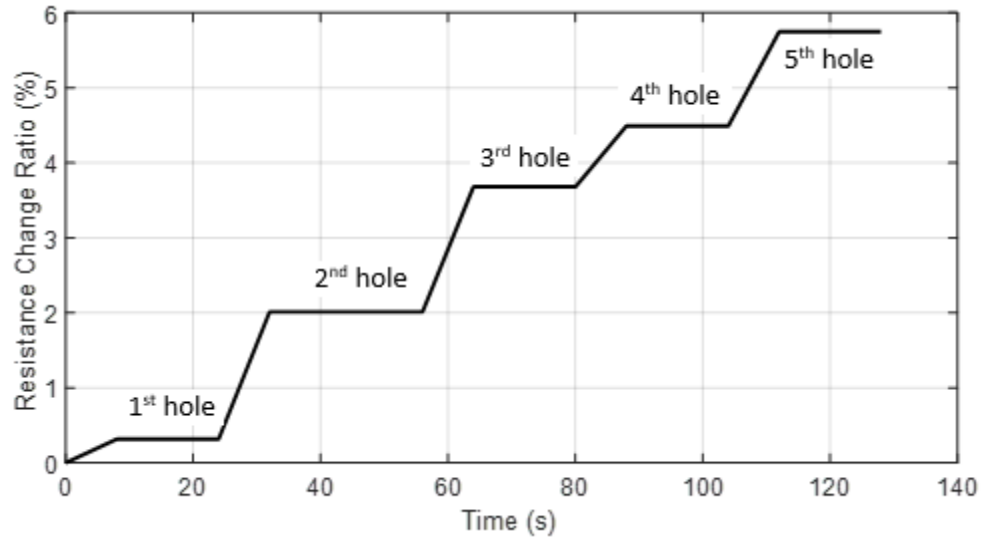


Figure 4.2 Resistance change ratio by addition of 3 mm hole statically in 3 inch \times 3 inch sensor.

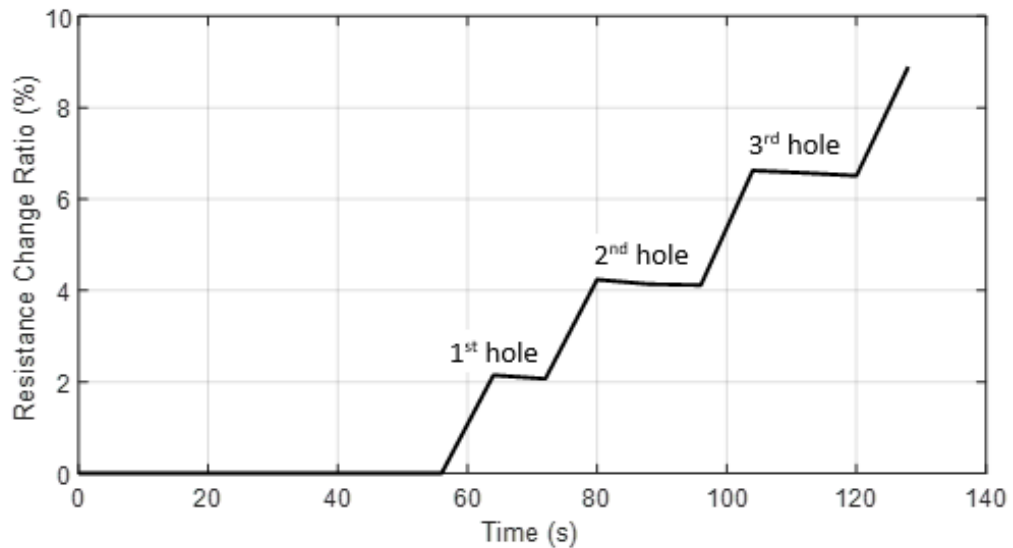


Figure 4.3 Resistance change ratio by addition of 4.5 mm hole statically in a 3 inch \times 3 inch sensor.

In case of the 3mm diameter hole, total of 5 holes were made. Addition of each hole resulted in a 1%-1.5% resistance change ratio. This can be attributed to the fact that the sensors were not held using any fixtures and other strains also contributed to the results. On the other hand, when a hole of 4.5 mm diameter was made, each hole resulted

in a 2% resistance change ratio. Clearly the change in resistance ratio was proportional to the size of damage.

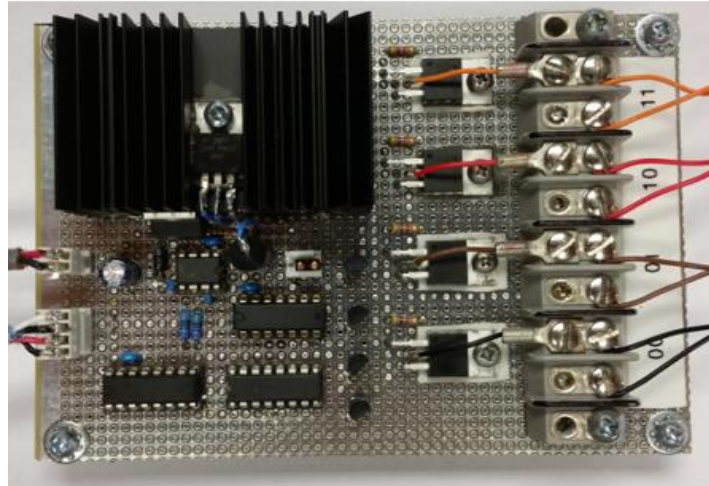


Figure 4.4 Circuit of four channel electronic control circuit.

4.3. Array of Sensors

The next step was to test an array of sensors for change in electrical resistance as damage was simulated and the change in voltage was recorded using the DAQ system. An array of four sensors measuring 2 inch \times 2 inch was tested with a control circuit (Figure 4.4), which periodically passed 0.5A current through each sensor in the array one-by-one, using a switching mechanism. The circuit was set to send the current to each sensor for two seconds only and then move on to the next sensor in the array. DAQ system recorded the voltage across the sensor for these 2 seconds and an average of hundred readings were taken. This practice aided in the preparation of circuit designs and LabVIEW codes for the hypervelocity impact test (HVIT). The same concepts were applied to test an array of nine sensors during the HVIT.

4.4. Test Fixture Design and FEA for Hypervelocity Impact Test

Figure 4.5 shows the design of the test fixture for the hypervelocity impact test. The hybrid sensors were glued on a style 7781 E fiberglass dry fabric and the fabric was held (glued) between two photo frame plates measuring 8 inch \times 8 inch with a cut-out measuring 6 inch \times 6 inch. Four holes were drilled at 7 inch \times 7 inch from the center. Four such layers (held between 8 frames) were held together by 1 ft long high-strength steel 3/8 inch-16 threaded rod. Steel hex nuts and washers were used to position each layer. Each layer was 2 inch apart from the other layer. The frames were cut from 1/8 inch Aluminum 6061 sheets.

4.5. Hypervelocity Impact Simulation: Baseline Model

A preliminary hypervelocity impact simulation was designed in LS Dyna. Since the sensors did not contribute to the strength of the target stack, only fiberglass was modeled and discretized for the analysis. The fixture frames and the fabric were discretized using shell elements. In the actual set-up, the glass fiber carried the sensors and was glued and clamped between the frames. This was simulated by maintaining mesh connectivity at all four edges of the fabric and the frames. Appropriate thickness was assigned to each component. Each layer was 2 inch apart from the other layers.

The projectile was also discretized using shell elements and was assumed to be rigid. It was given an initial velocity of 7 Km/s. The frames were fixed at their position by using nodes on all edges of each frame and constraining them with single point constraints (SPC_NODE_SET) in the global coordinate system.

AUTOMATIC_SURFACE_TO_SURFACE type contacts were used to transfer forces between the projectile and glass fiber. As shown in Figure 4.6, a biased mesh was created

in the center of each layer to capture the impact mechanics better.

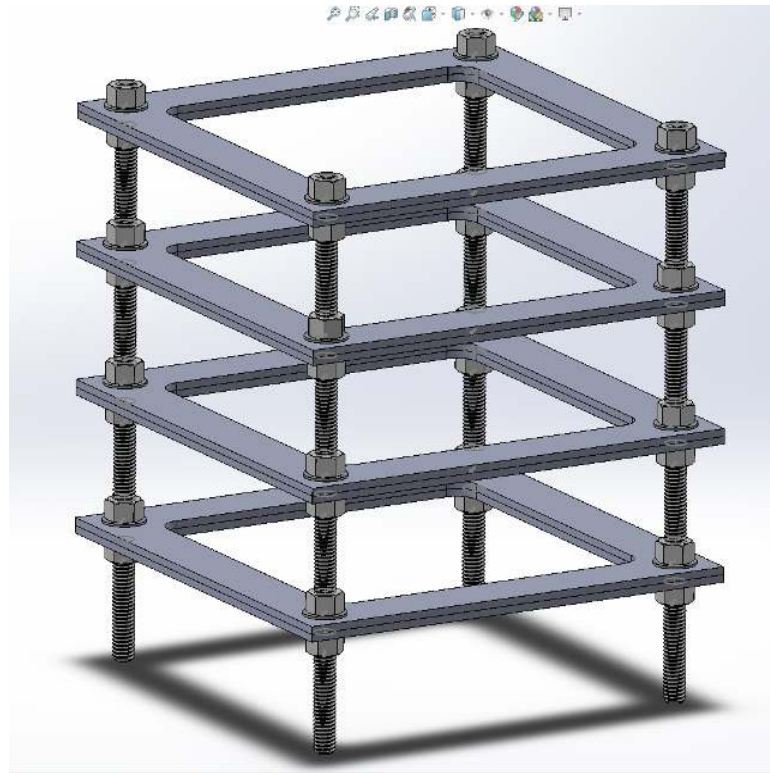


Figure 4.5 Fixture Design.

Besides, the mesh of the projectile was created much coarser than the target layers in order for the contact to work efficiently.

4.6. Assumptions

Mainly two assumptions were made to simplify the model. Firstly, the projectile's size was exaggerated to inch diameter so that reasonable mesh size could be used. Since the mesh size on the projectile needs to be coarser than the target, using the actual size of the projectile would require extremely fine mesh. The second assumption has been made for the material model for glass fiber. In order to model woven fabrics, two approaches have been used by researchers. One of them is to model and mesh each fiber so that a simple material model can be assigned to it (Nilakantan, Keefe, Bogetti, & Gillespie Jr,

2010). The other is to treat the fabric as a continuum material and use an appropriate material model which can capture the right damage mechanics (Shahkarami & Vaziri, 2007; Lim, Shim, & Ng, 2003). The second approach has been taken for this simulation.

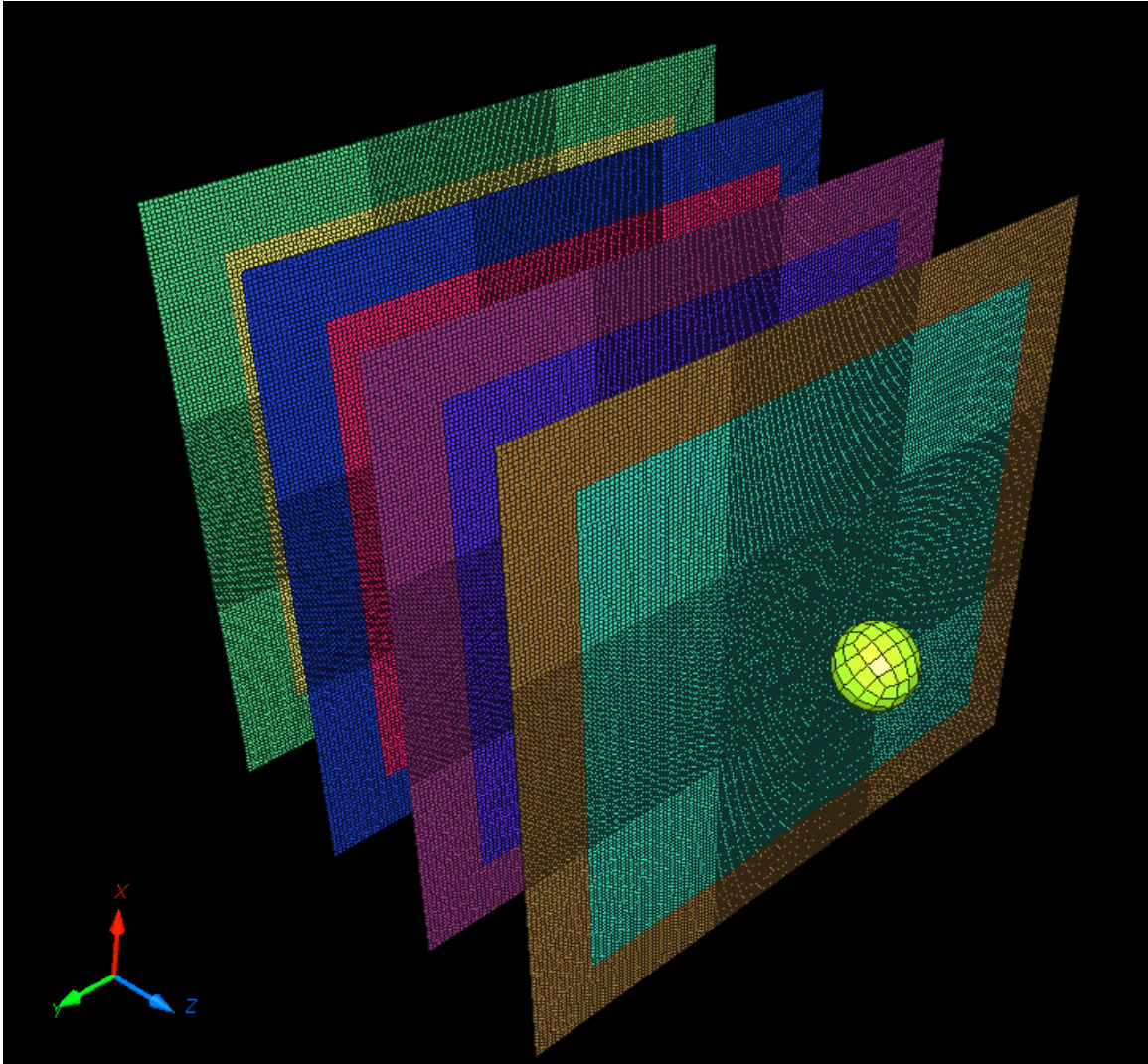


Figure 4.6 Finite Element model of test article.

4.7. Material Models

In order to achieve realistic results, the most important factor is to use the right material model and material properties. Kinematic_Plastic material model (MAT_03) was chosen for aluminum frames. To model the woven fabric, the composite failure

model Chang Chang (1987) model, MAT_COMPOSITE_DAMAGE (MAT_022) was first considered due to its simple approach. However, it provides various failure modes due to in-plane stresses only. It is a two-dimensional failure model which neglects out-of-plane shear and normal stresses. This might be enough for composites under in-plane loading but would fail to capture transverse impact failures (Yen, 2002).

MAT_LAMINATED_COMPOSITE_FABRIC (MAT_58) is another popular choice used to model composite materials with unidirectional layers, complete laminates, and woven fabrics. It was used to successfully predict debris impact damage due to the reinforced carbon-carbon leading edge panels of the space shuttle Columbia (Carney, Melis, Fasanella, Lyle, & Gabrys, 2004). This model is a continuum damage mechanics material model that requires stress-strain curves as input to define mechanical behavior in tension, compression, and shear. The damage model is defined by maximum strain for layer failure, beyond which the elements are eroded from the model. It must be noted that this material model does not represent individual fibers but represents each layer in the laminate (Jackson, Fasanella, & Littell, 2017).

A finite element model was first prepared with simple material models to establish a baseline. This step helped in ensuring that the boundary conditions, initial conditions, and contacts were working. Therefore, Kinematic_Plastic model was assigned to frames and the woven fabric. Failure strain for eroding elements was used as the failure criterion. The results are presented in the following sections. Table 4.1 shows material properties used for the simulation.

Table 4.1

Material Properties Used in the Simulation (Matweb.com, 2015).

Material Property	Value
Mass Density	2.8 g/cm ²
Young's Modulus	710 kbar
Poisson's Ratio	0.33
Yield Stress	5.03 kbar
Tangent Modulus	6.03 kbar
Failure strain for eroding elements	0.046

4.8. Results of the baseline model

Figure 4.7, Figure 4.9 and Figure 4.7 show the results of the impact simulation on the baseline model. GLSTAT data from the model (Figure 4.7) shows that the total hourglass energy is less than 5% of the total energy, which is indicative of a stable simulation. The loss in total kinetic energy is seen to be compensated by increase in the sliding energy (Figure 4.7) and the increase in the internal energy of each layer (Figure 4.8). It should be observed that the energy dissipated by each layer is negligible in order of magnitude. Sliding energy refers to the sum of slave (target) and master (projectile) energy in the contacts. Moreover, kinetic energy is appropriate to the initial velocity of the projectile. This shows that the baseline model is stable. Figure 4.9 shows a snapshot of the animation for finite element simulation.

The next step would be to use the more complicated composite material model. However, material properties required for the inputs were not known to the manufacturer as the company does not perform any tests on the material. Besides, all the work done on

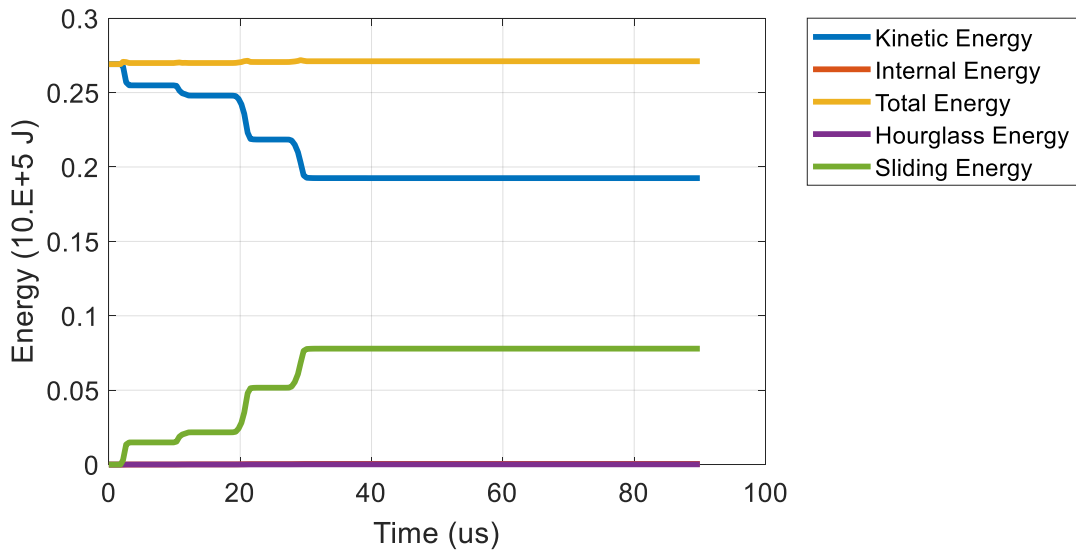


Figure 4.7 Energy data from the baseline model

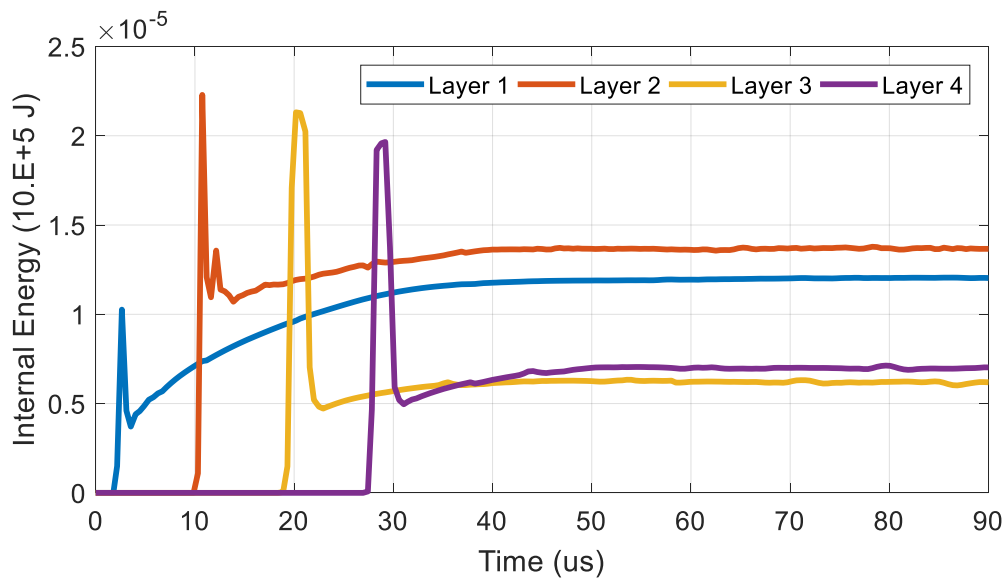


Figure 4.8 Internal energy absorption by each layer

similar materials has been done at low-velocity impacts. Therefore, material characterization tests are required. In general, tensile tests would be needed in which coupon fibers are oriented at 0, 90 and +-45degrees. However, since in this case, the same fiber is woven together, tests in 0 or 90 degrees, and +- 45 degrees would suffice. The former would provide data on longitudinal properties while the latter would provide

data for shear properties. A simple finite element model of the material characterization test would then be executed to ensure that the material model replicates the material behavior with these inputs.

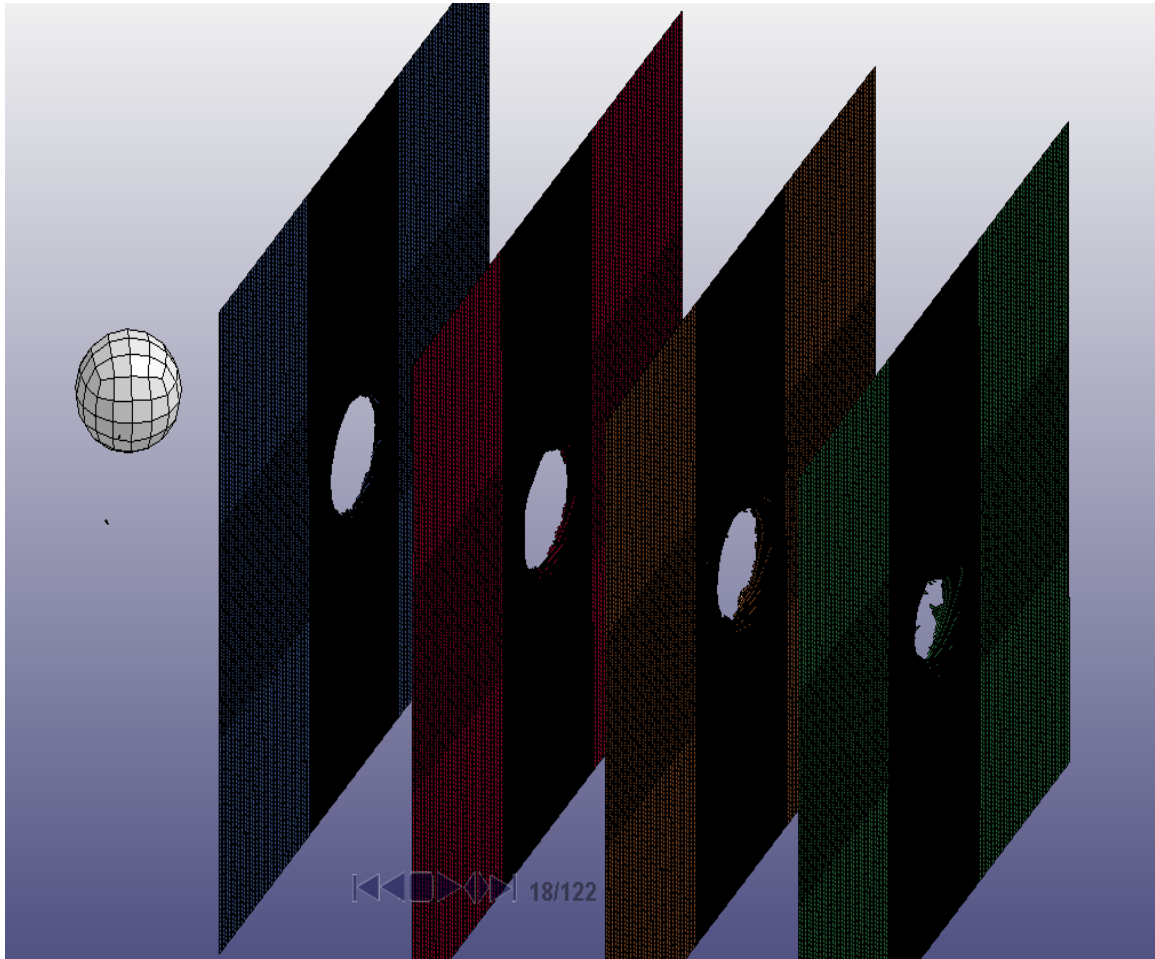


Figure 4.9 Snapshot of hyper velocity impact simulation of baseline model

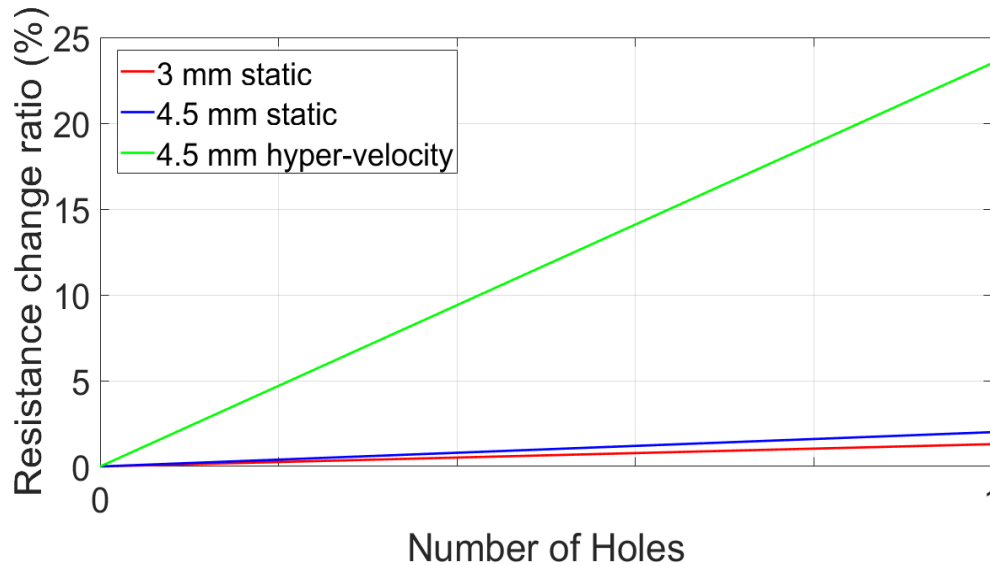


Figure 4.10 Comparison of response of sensors to static and dynamic loading

4.1. Discussion

Holes of 3 mm and 4.5 mm were drilled in the sensors and results were plotted (Figure 4.10). The sensors gave detectable and measurable results. An array of four sensors was tested with periodic scanning circuit and LabVIEW codes, and the change in voltage was captured effectively. Results were compared based on:

1. Size of the hole during static testing
2. Static and hypervelocity impacts

It was seen that the response of sensors during the hypervelocity impact test was 10 times that of the response recorded statically. The addition of a 3mm hole statically caused approximately a 1.3% resistance change ratio, the addition of a 4.5 mm hole statically caused a 2% resistance change ratio, whereas a projectile of 3mm diameter caused a hole of 4.5 mm diameter that resulted in 23.5 % resistance change ratio when shot at 7km/s at the sensors. Figure 4.10 shows a comparison of the three cases. This indicates that the sensors are more responsive and sensitive to dynamic loading.

The baseline finite element model presented here is a preliminary model and only helped in understanding and recognizing the process of completing the hypervelocity impact simulation. The results could not be directly used or related to the experiments as accurate material properties were not used. The material characterization tests could not be carried out, as achieving dynamic tensile properties at such high strain rates would require special equipment, which is out of the scope of present work and is recommended as future work.

5. Hyper Velocity Impact Test

The following sections present hypervelocity impact tests conducted at University of Dayton Research Institute (UDRI), Ohio. Working of a light gas gun, importance of conducting impact tests, description of projectile, instrumentation and data acquisition are explained in detail. Finally the results are discussed and compared with similar works conducted in the past.

5.1. Hyper-Velocity Impact Test

The three most important requirements for a successful hypervelocity test as stated by the University of Dayton Research Institute are:

- 1) A system to launch and accelerate the projectile at desired velocity.
- 2) Sabots capable of supporting the projectile subjected to launch loads due to high g-accelerations and enabling easy release of the projectile without disturbing its flight path.
- 3) A means for clear capturing of the discarded sabot without disturbing or damaging the projectile or target.

5.1.1. Test Range

This test was conducted on Range 4, a 50mm/20mm two-stage, light-gas gun located in the Impact Physics Laboratory at the University of Dayton Research Institute. A photograph of the gun is shown in Figure 5.1 (Range 4 is on the left). It has a 19- foot long, 50 mm bore diameter first stage, called pump tube, and a 16- foot long, 20 mm bore diameter second stage called launch tube. The projectiles were installed in a plastic sabot



Figure 5.1 Test Range at UDRI hypervelocity impact laboratory (Courtesy of UDRI). with a cavity sized to fit the projectile. This launch package was then loaded into the launch tube and fired at the test article mounted in the gas gun chamber shown in Figure 5.2. A brief description of the firing cycle is shown in Figure 5.3. Axially split, aerodynamically- separating plastic sabots were used for the test. Front of the sabots has integral scoops that react with the range pressure and cause the petals to start rotating. The petals eventually separate from the projectile as they travel. As the separating projectile and sabot come close to the target, the projectile passes through the hole in a heavy steel stripper plate and sabot is stopped by the impact on the plate around the hole. Figure 5.4 shows a sabot and a spherical projectile.

After launch, the sabot was stripped away from the projectile by a sacrificial steel sabot stripper plate located 18 feet from the launch tube muzzle. The projectile was in free flight to the target for approximately 24 feet. This free-flight distance permitted accurate measurement of the projectile velocity with laser-photodetector stations positioned along the projectile flight path. The tests were performed in a near vacuum

with approximately 11 mm of air pressure.

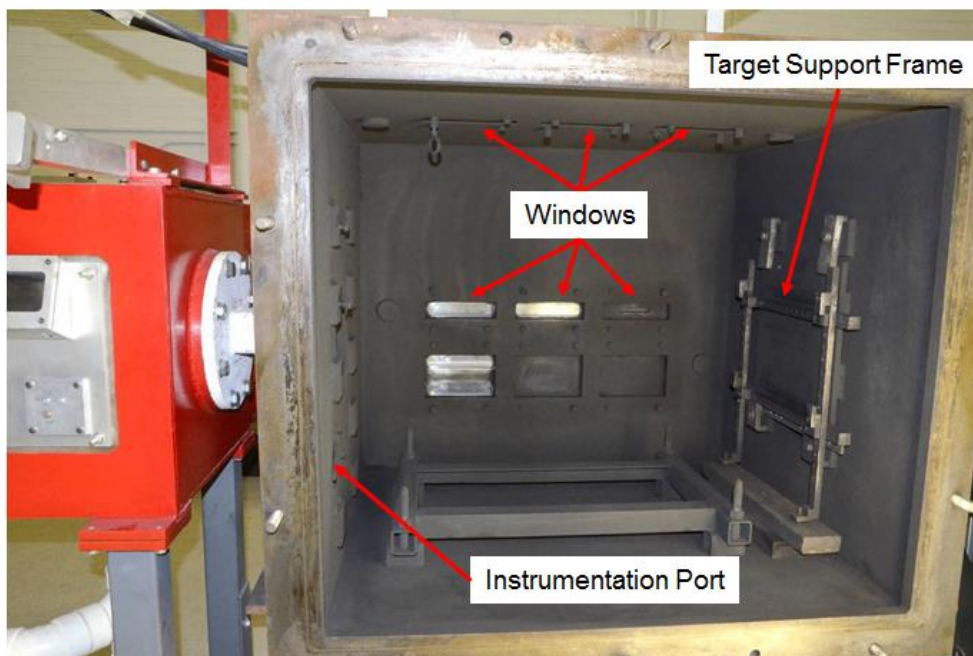


Figure 5.2 Gas gun chamber at UDRI, Impact Physics Laboratory, Range 4 (Courtesy of UDRI).

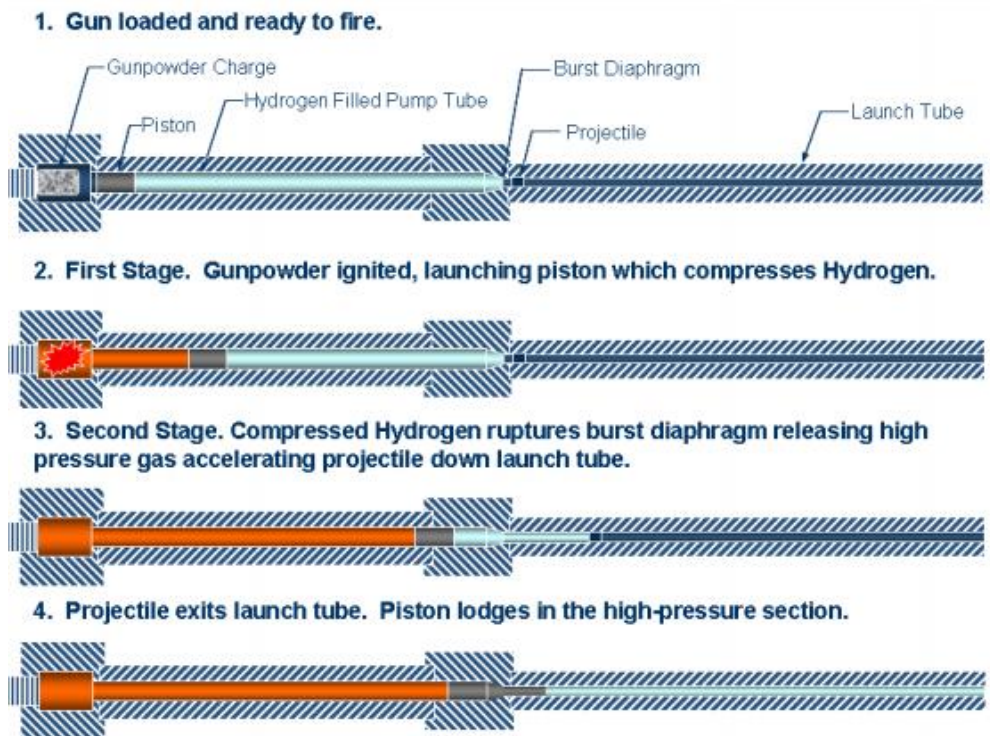


Figure 5.3 Two-stage light gas gun firing cycle (Courtesy of UDRI).

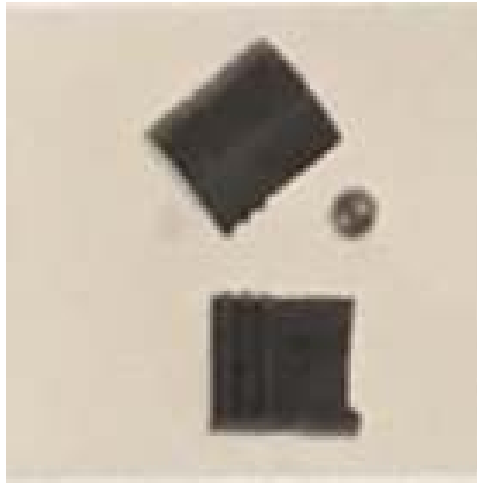


Figure 5.4 Sabot and spherical projectile (Courtesy of UDRI).

5.1.2. Test Articles and Test Setup

The full test article was similar to the micrometeoroid orbital debris protection layers commonly used for the inflatable space habitat structures. The main objective of this experiment was to test the functionality of sensors in arrays, to exhibit the capability to detect depth of damage and location of the depth in a plane. This was achieved by assembling various layers of sensors in the following way.

The four-layer test article consisted of three hybrid nanocomposite impact sensors layers and one structural layer. Each impact sensor layer was composed of Kapton®-covered flexible CNT-GNP sensor layer bonded onto thin fiberglass fabric, which was sandwiched between two aluminum perimetric frames. The four layers were placed two inches apart but held together by four all-thread rods through the corners of the frames. Top and front views of the test article are shown in Figure 5.5 and Figure 5.6 respectively.

Two tests were performed with a different sequence of sensors and different sizes

of projectiles. For the first test, although the effective sensing area of each layer was 6 inch by 6 inch, the first layer only contained single 2 inch by 2 inch CNT-GNP sensor at the center of the layer as the impact point was predetermined.

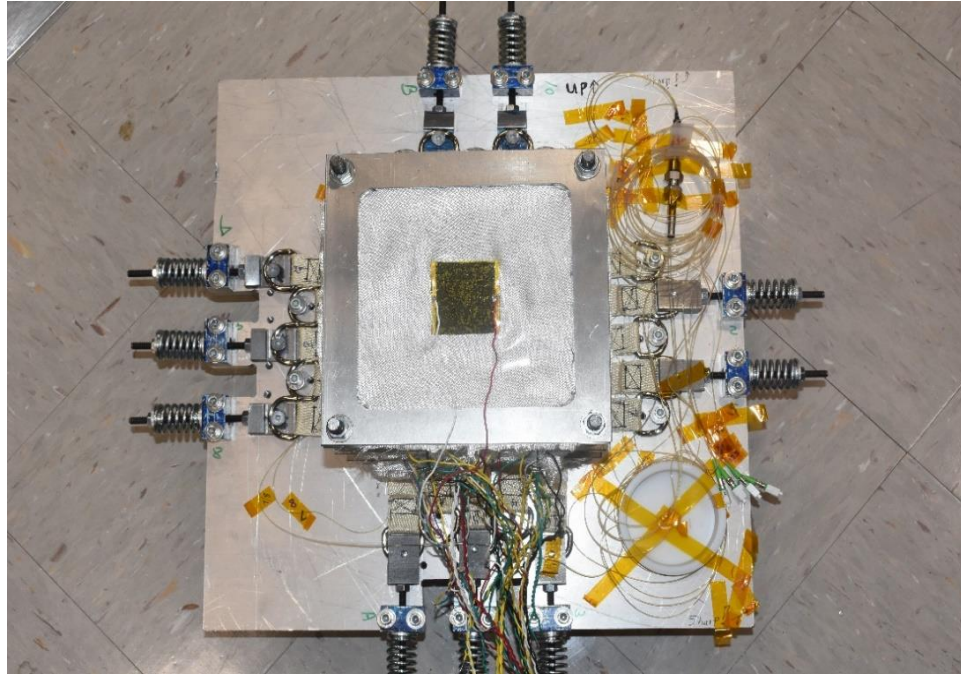


Figure 5.5 Top view of the test article

The second layer consisted of an array of 9 of those hybrid sensors covering the entire sensing area. The third layer was arranged the same as the second layer, but the hybrid sensors were replaced by the inkjet-printed CNT water-based sensors. The last structural layer was a Vectran webbing, mounted to a fixture that had springs attached to the webs to provide a tensile load on the webs. Woven into the webbing were fiber optic bundles. This layer was provided by Luna Inc. The projectile used for this test was 3.17 mm diameter.

Another similar experiment was conducted using a 4.7 mm aluminum projectile. The first layer for this test consisted of one inkjet sensor in the center of the fabric. The second layer consisted of an array of 9 inkjet-printed sensors while the third layer

consisted of 9 hybrid sensors. Another change made to the test article was an aluminum plate with a hole in the center bonded to the first frame. This was done based on visual inspection of the test article after the first test. This arrangement avoided loss of data due to damage to the surrounding fiberglass fabric on the first layer.

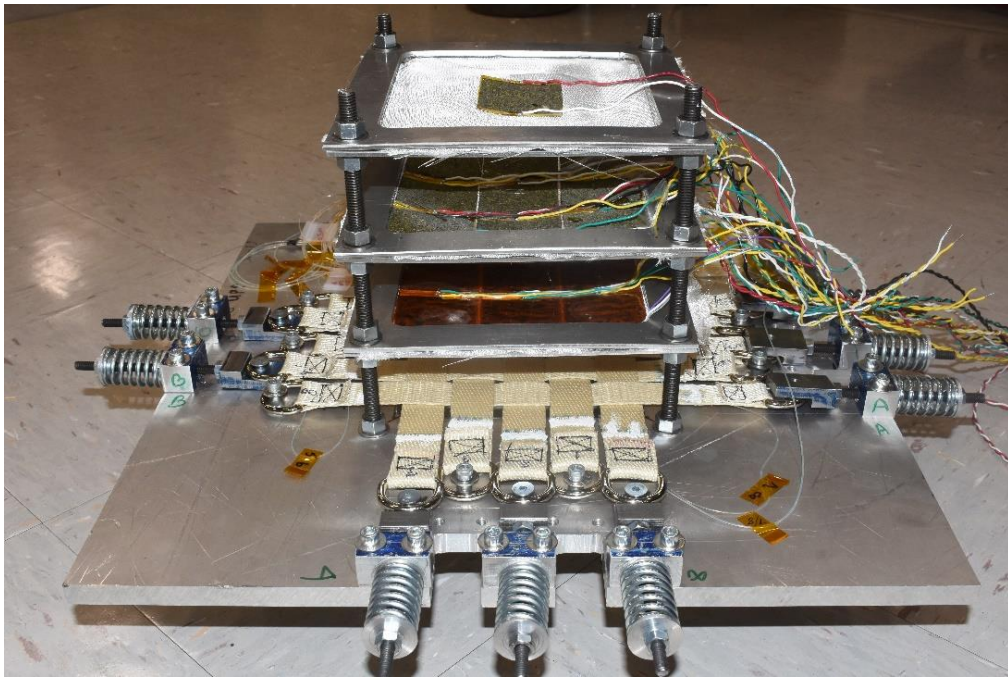


Figure 5.6 Various layers in the test article

The test articles were mounted to a fixture attached to the rear wall of the target chamber using extensions of the all-thread rods used to assemble each test article and suitable spacers and nuts as shown in Figure 5.7.

5.1.3. Projectile Description

The projectiles used for the tests were 2017-T4 aluminum spheres. Projectile diameters were measured with a micrometer and their weights were determined using a Mettler Model H10 analytical balance with an accuracy of a ± 0.0002 gram. The diameter of the projectile for the first test was 3.178 mm, while for the second test it was 4.76mm.

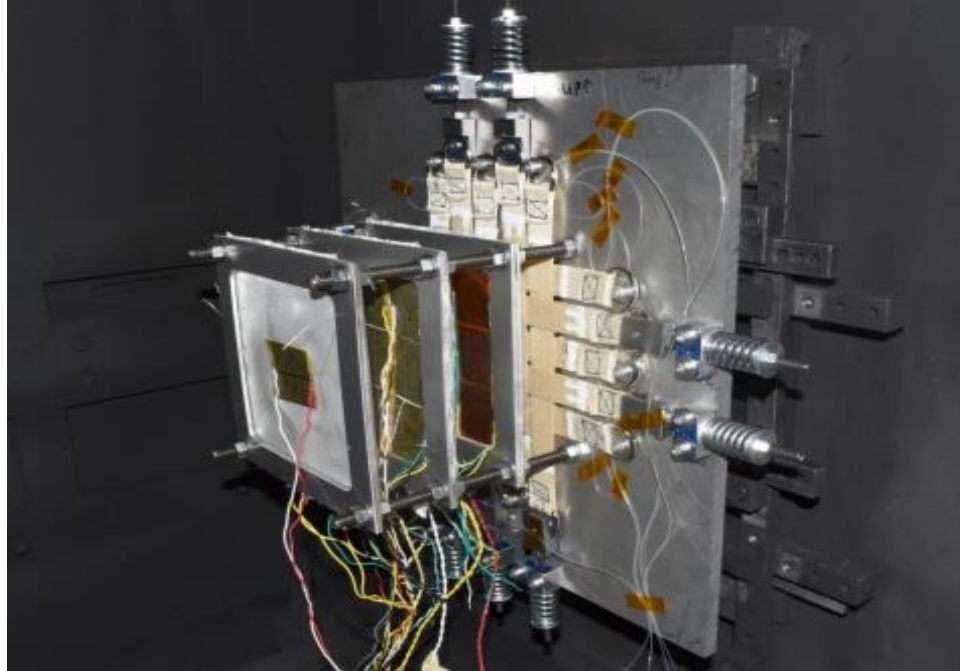


Figure 5.7 Test article Setup

5.1.4. Instrumentation

Despite all the instrumentation performed to gather data during the test, the resistance of all the sensors used was recorded before the start of the test and after the end of the test as precautions. Periodic sensing was performed on an array of 9 hybrid sensors using a multichannel circuit (Figure 5.8) by sending a 0.5 A current to each sensor in a 2-second sequence. The circuit consisted of 9 channels that were addressed using 4 address lines. The voltage signal from each of the sensors was recorded using a LABVIEW code (Figure 5.9) in order to monitor their resistance. Change in voltage for the single hybrid sensor on the first layer was recorded before and after the impact using a multimeter. The circuit was placed inside the chamber and was covered with a plastic shielding to protect it from any potential damage from the impact debris.

BNC feedthroughs and Swagelok fittings were used to bring cables in and out of the test chamber as shown in Figure 5.10. The data collected from the impact tests also

included the projectile diameter and weight, the projectile impact velocity, verification of projectile integrity using flash radiography, and photographic documentation of the damage to the test articles. All data-recording instruments are calibrated annually to NIST traceable standards.

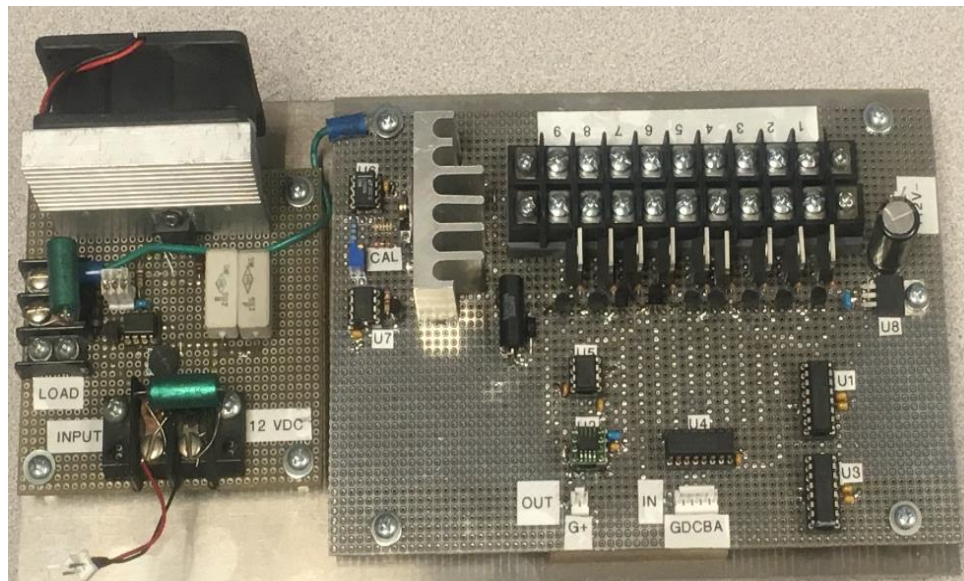


Figure 5.8 Circuit of nine channel electronic control circuit.

5.1.1. Velocity Measurement

The projectile velocity was measured with four HeNe laser-photodetector stations spaced over 159.63 inches. The last laser station was located roughly 60 inches from the target. Each laser projected a beam that intersected the projectile trajectory normal to the trajectory and illuminated an opposing photodetector station. When the projectile interrupted the beam, the interruption time was recorded by an HBM Genesis data acquisition system operating with a sampling rate of 10 MHz.

The projectile velocity was calculated by dividing the measured distance between any two sets of laser-photodetector stations by the time of flight between those two

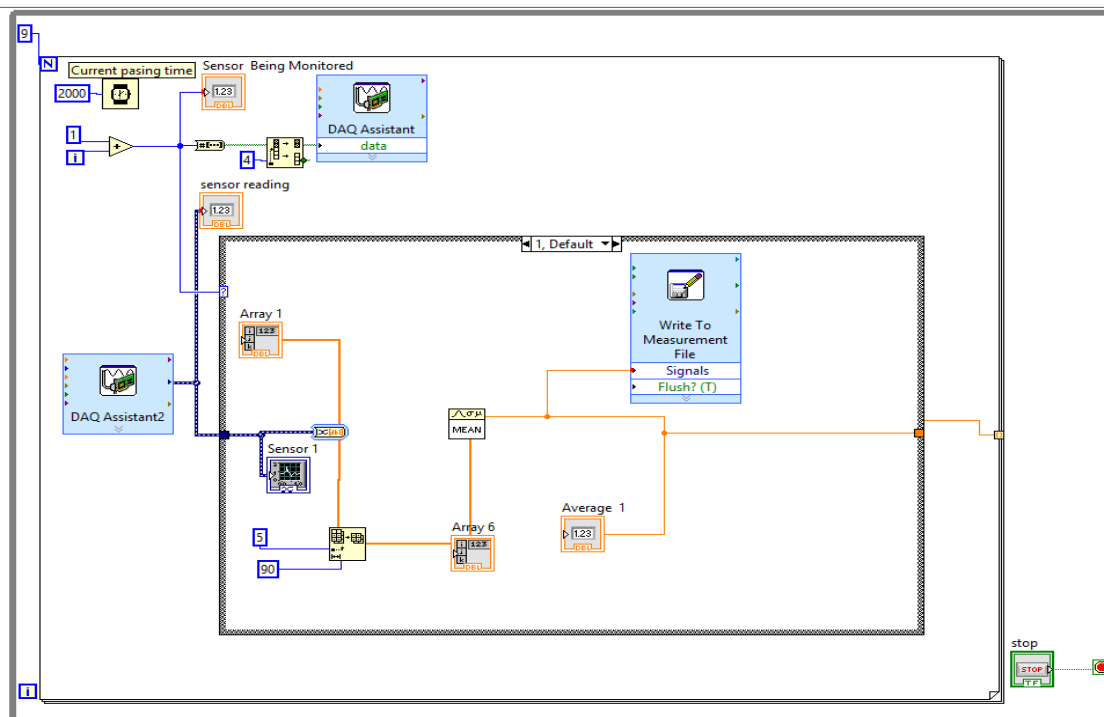


Figure 5.9 LabVIEW code for data acquisition of HVIT.

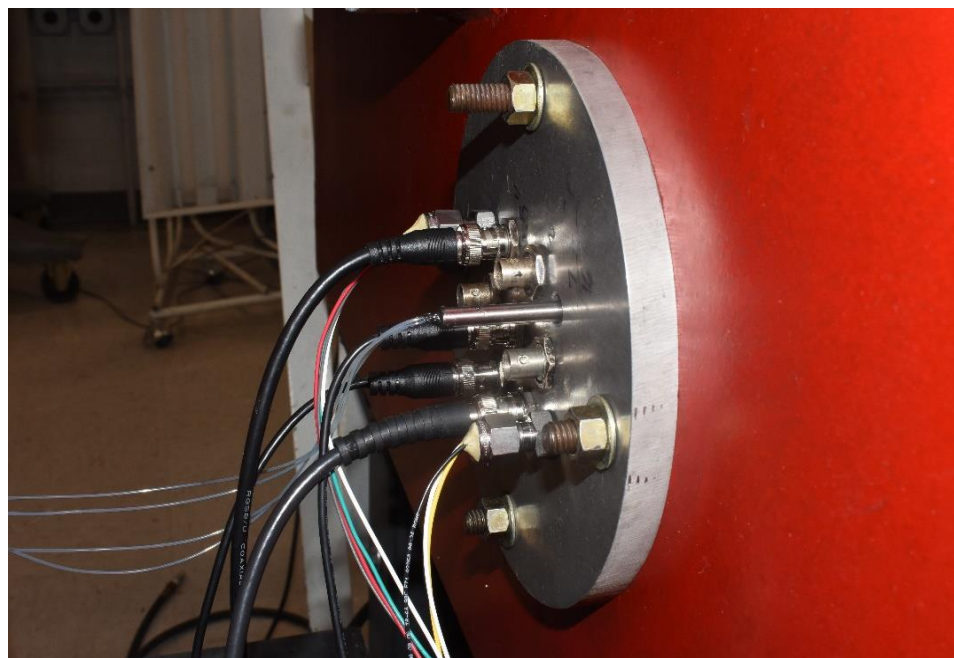


Figure 5.10 BNC feedthroughs and Swagelok fittings for instrumentation during the test. stations. The use of four laser-photodetector stations allowed UDRI to make up to six different computations of the velocity of the projectile with three of these being

independent measurements. Velocity measurement accuracy is better than 0.5%.

5.1.2. Flash Radiography

Projectile integrity was verified using a Scandiflash 150 kV, dual-head, flash x-ray system. Radiographs were made using Industrex Flex XL Blue Computed Radiography screens. The orthogonal pair of flash x-ray heads were used to capture images of the projectile after the sabot had been stripped and prior to impact with the target. “Firing” of the x-ray system was controlled using trigger pulses from time-delay generators which were “started” by signals produced by the passage of the projectile through the fourth laser-photodetector station. The appropriate time delays required to capture the views of the projectile, when it was over the film/screen, were preset prior to charging the x-ray system. Individual time delays were computed using the expected projectile velocity and the downrange location of the x-ray film with respect to the laser-photodetector station providing the “start” signal.

5.2. Impact Test Results

A total of 2 successful tests were performed. A summary of the test conditions and test results for the test series are presented in Table 5.1.

Table 5.1

Summary of the Impact Tests

Test No.	Projectile Material	Projectile Diameter (mm)	Projectile Mass (g)	Impact Velocity (km/s)	Impact Energy (J)	Results
1	2017-T4 Al	3.178	0.0458	6.99	1,118	All three fabric layers penetrated with spray on the fourth layer
2	2017-T4 Al	4.760	0.1583	6.88	3,750	All three fabric layers were penetrated with small perforation on the fourth layer

5.3. First Impact Test

During the first test, the first layer consisted of a single hybrid sensor in the center of the test article, while the second layer carried an array of 9 sensors. The third layer carried an array of 9 CNT printed sensors. Figure 5.11 and Figure 5.12 show the test article before and after impact. Damage was seen on the first three layers. The fiberglass fabric on the first layer carrying a single sensor was damaged due to shock and high pressure.

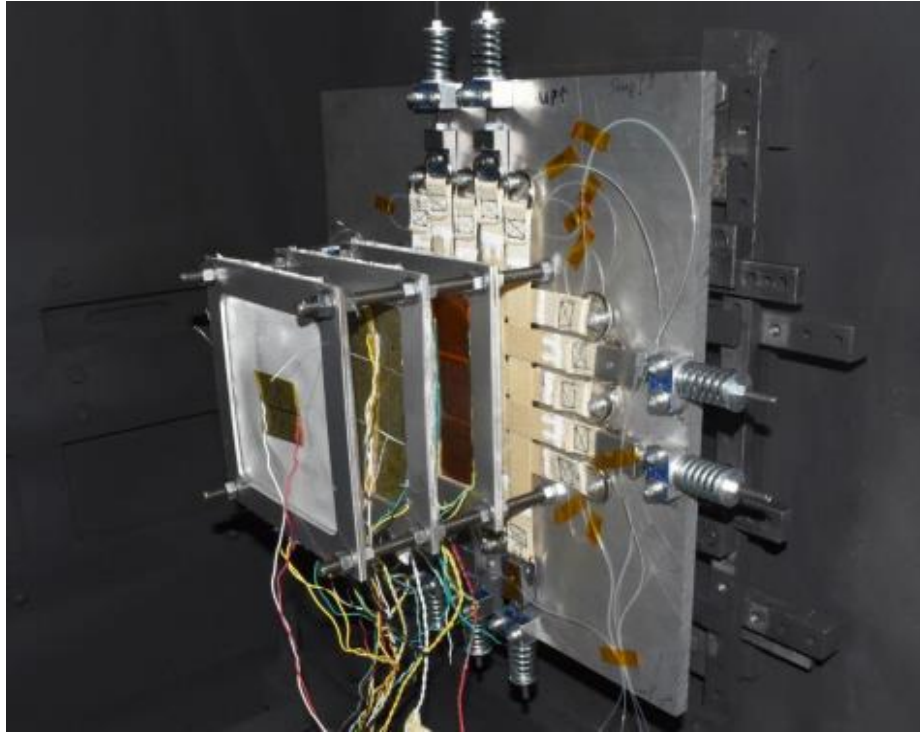


Figure 5.11 Test article before the impact

Figure 5.13 shows the nomenclature for the array of 9 hybrid sensors. The sensors were marked 1 to 9 from top left to bottom right as shown. Figure 5.14 shows the damage on the first layer and the projectile used for the test. Figure 5.15 through Figure 5.20 show front and back sides of all the layers after impact. The single sensor in the center on the first layer suffered damage of diameter 4.66 mm (Figure 5.15 and Figure 5.16). Figure 5.17 and Figure 5.18 show front and back side of the second layer of 9 hybrid sensors after the impact. A damage measuring 20.2 mm was observed on sensor 5 in this layer. Figure 5.19 and Figure 5.20 show the front and back sides of the nine CNT printed sensors after impact. The electrodes of sensors 4, 5 and 6 were severed into two due to the size of the damage. No resistance measurements (infinity) was obtained after the test on those sensors.

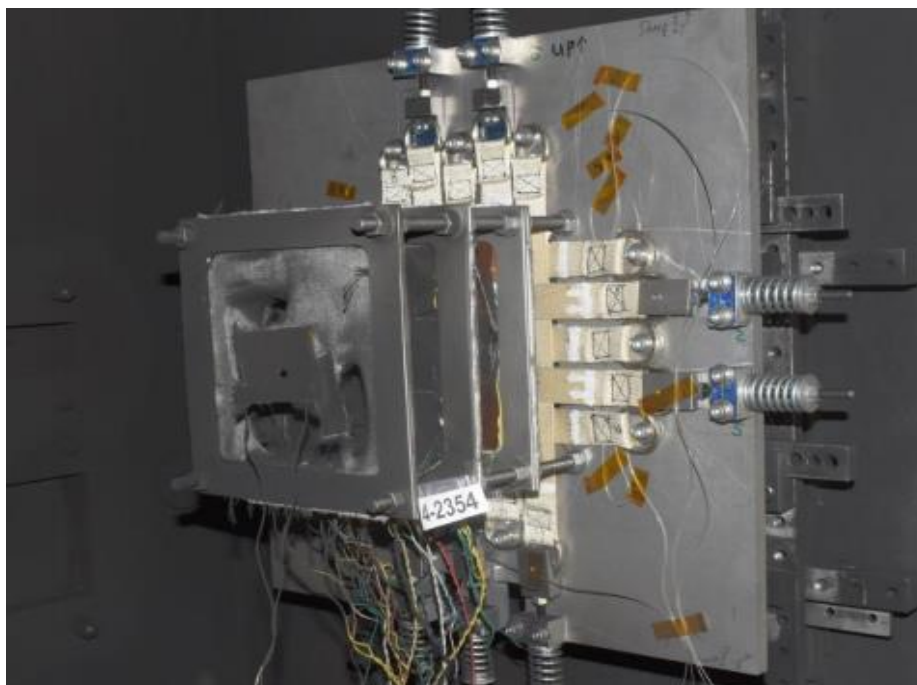


Figure 5.122. Test article after the impact

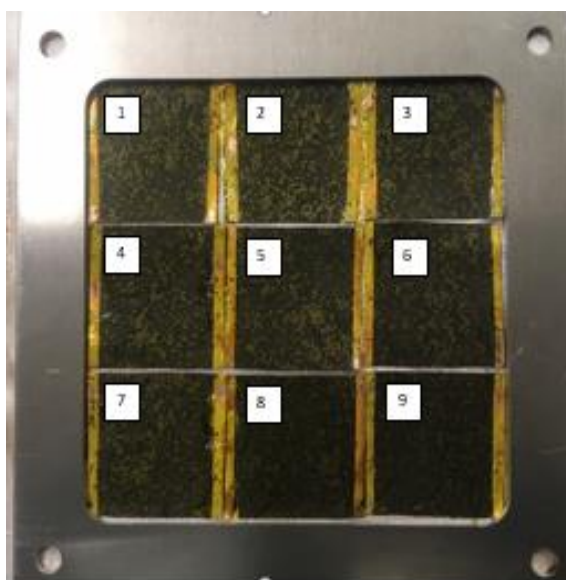


Figure 5.13 Nomenclature used to recognize the hybrid sensors in an array

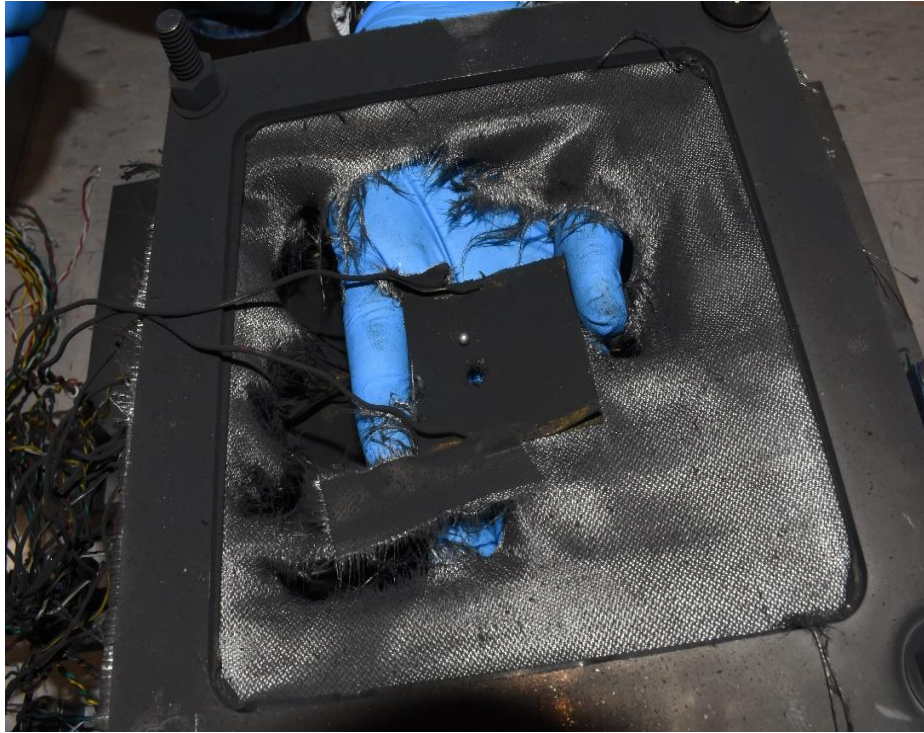


Figure 5.14 Damage on the first layer (hybrid sensors) and the projectile after the first test

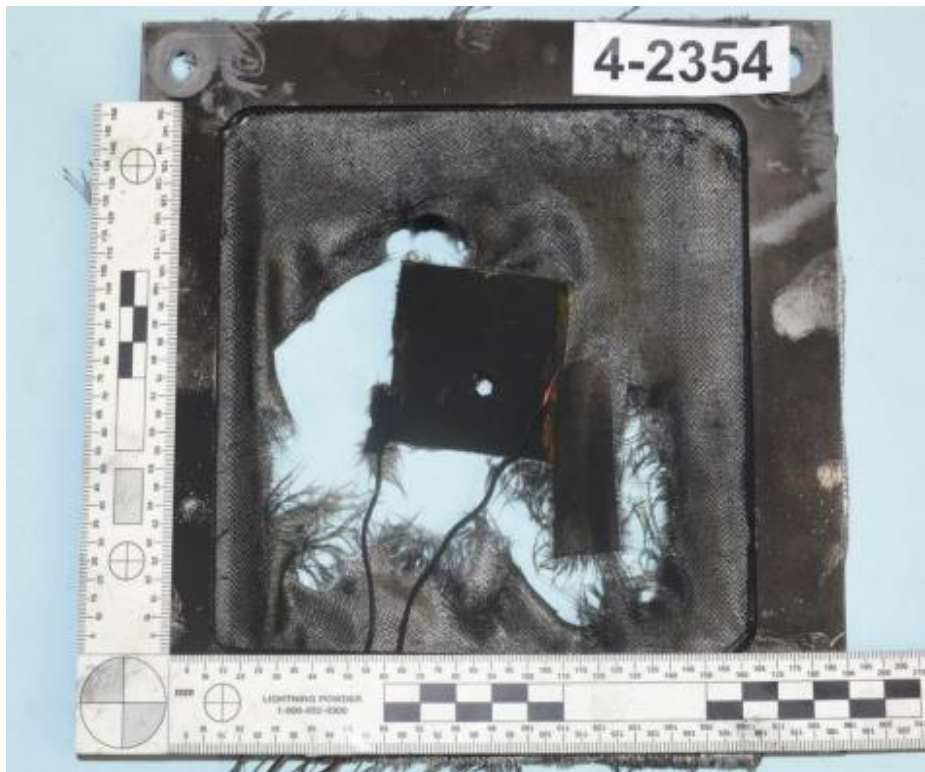


Figure 5.15 Front side of the first layer (hybrid sensors) after first test

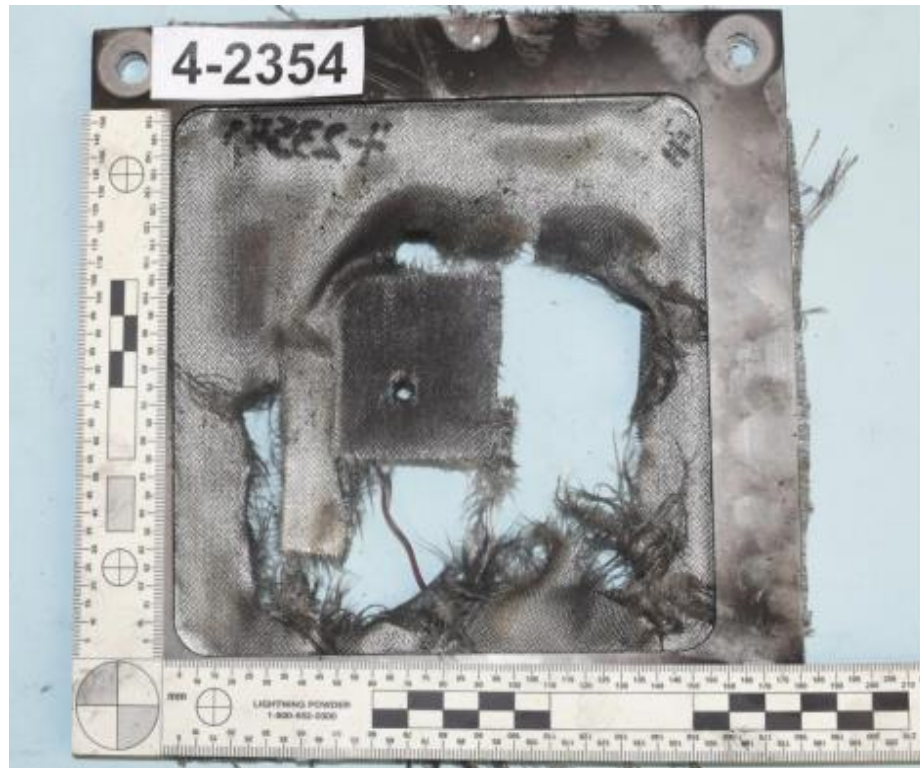


Figure 5.16 Back side of the first layer (hybrid sensors) after first test

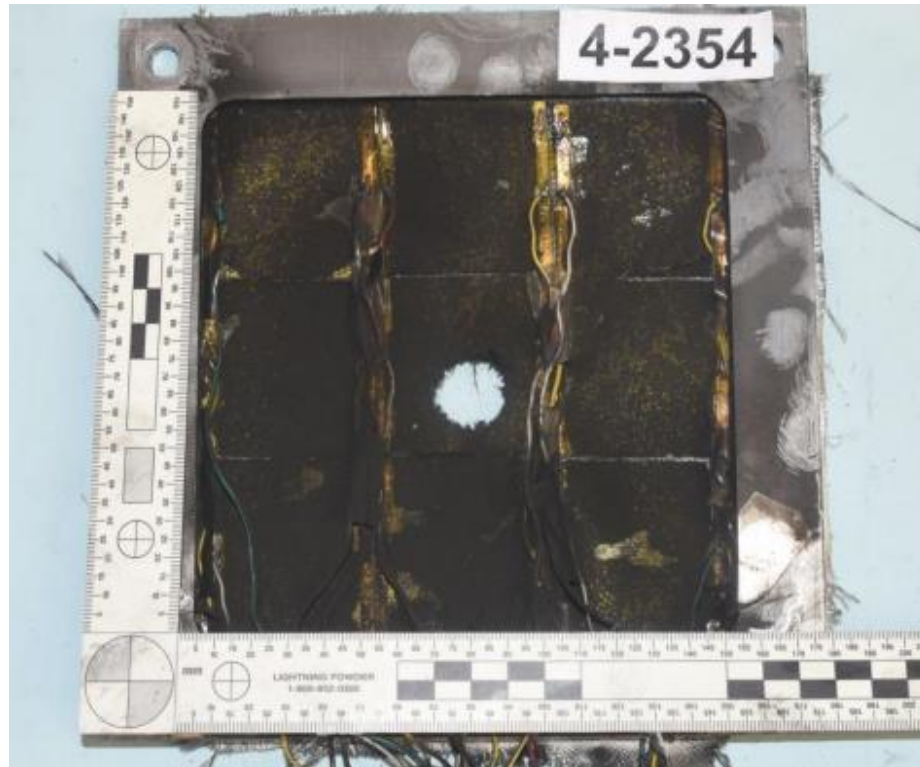


Figure 5.17 Front side of the second layer (hybrid sensors) after first test



Figure 5.18 Back side of the second layer (hybrid sensors) after first test

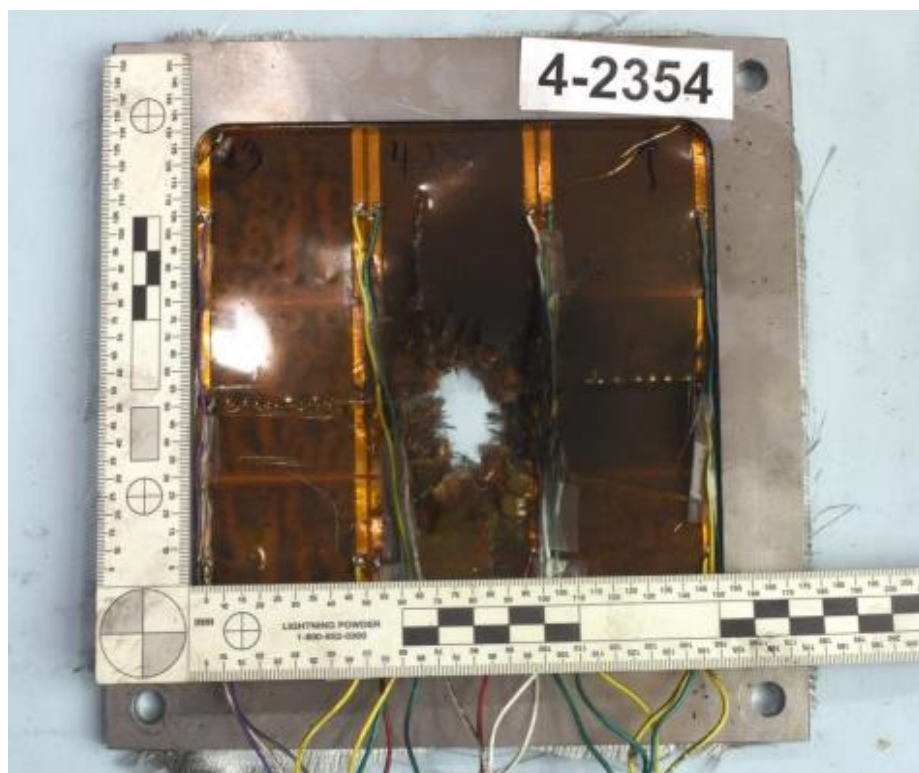


Figure 5.19 Front side of the third layer (ink jet printed sensors) after the first test



Figure 5.20 Back side of the third layer (ink jet printed sensors) after the first test

5.4. Resistance Measurement of Hybrid Sensors

The resistance of the single sensor on the first layer changed from 3.65 ohms to 4.51 ohms. Change in resistance ratio was calculated and was found to be 23.5%. Figure A.1 through Figure A.9 in the appendix show the percentage change in resistance which was derived from real-time voltage recordings during the experiment. Change in resistance for sensor 5 on the second layer was recorded by the data acquisition system and was found to be 150%. This is shown in Figure A.5 in the appendix. Although the other eight sensors were not impacted by the projectile, it was observed that they experienced some strain as the projectile hit sensor 5. This strain could have been caused by various factors like pressure and shock waves. Figure 5.21 shows the strain in the form of resistance change ratio in the plots for 9 sensors on the second layer.

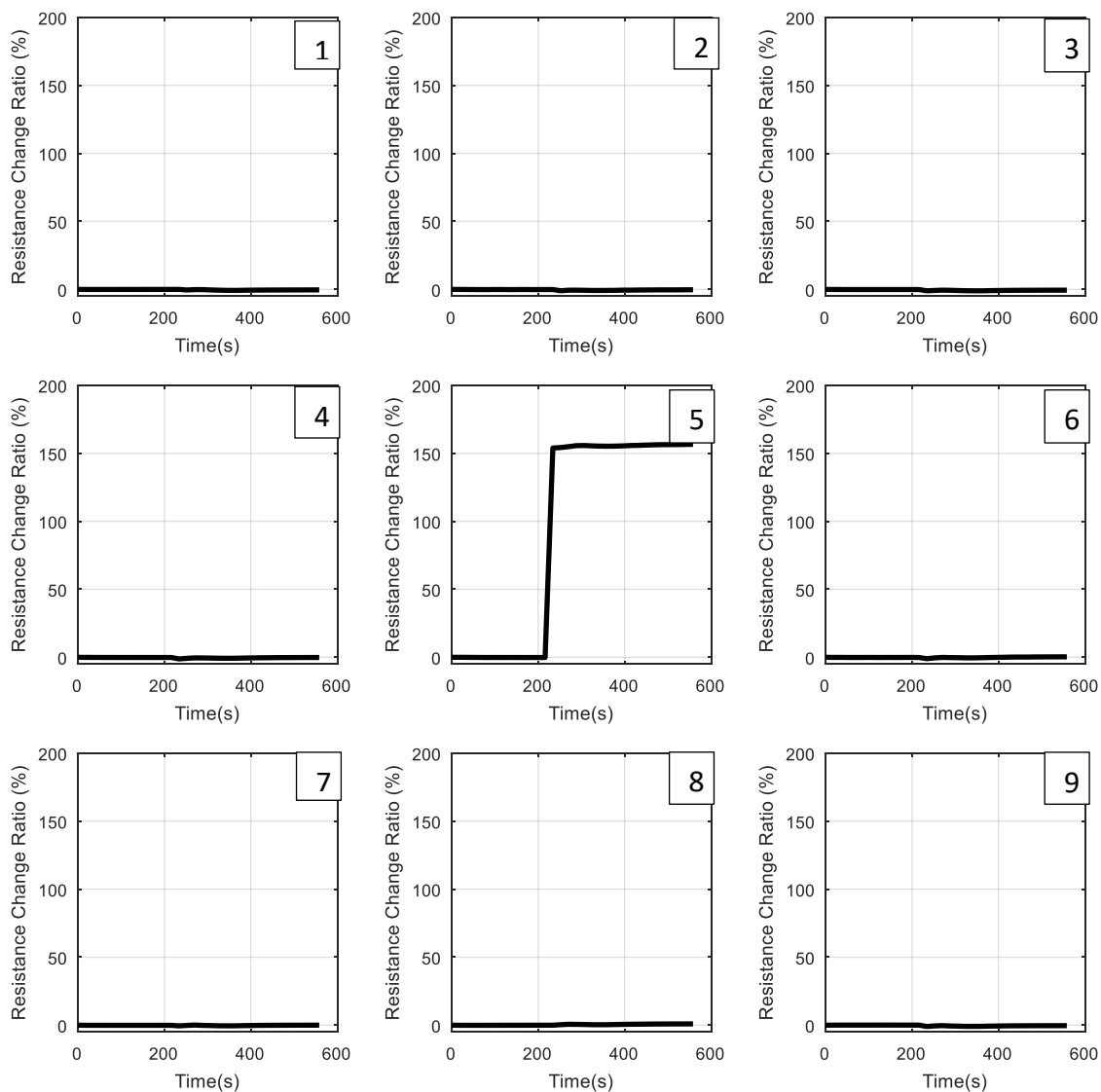


Figure 5.21 Response of different sensors during first HVIT.

5.5. Second Impact Test

For the second test, the array of 9 hybrid sensors was placed on the third layer while one CNT inkjet-printed sensor and 9 CNT inkjet-printed sensors were placed respectively on the first and second layers. Figure 5.22 and Figure 5.23 show the test article before and after impact. This arrangement gave a clear picture of the extent of damage on sensors depending on their location within the layers of inflatable habitats. Figure 5.24 and Figure 5.25 show front and back side of the CNT inkjet-printed sensor on

the first layer after the impact. Damage of size 6.07 mm was observed on the sensor.

Figure 5.26 and Figure 5.27 show front and back side of the 9 CNT inkjet-printed sensor on the second layer after the impact. Clean damage of size 15.31 mm was measured on the middle CNT inkjet-printed sensor (sensor 5). Figure 5.28 and Figure 5.29 show front and back side of the hybrid sensors on the third layer after the impact. The nomenclature used for the previous test was followed to recognize the sensors. It was observed that the damage caused to the array of hybrid sensors was much larger as compared to the damage caused on the first and second layers.

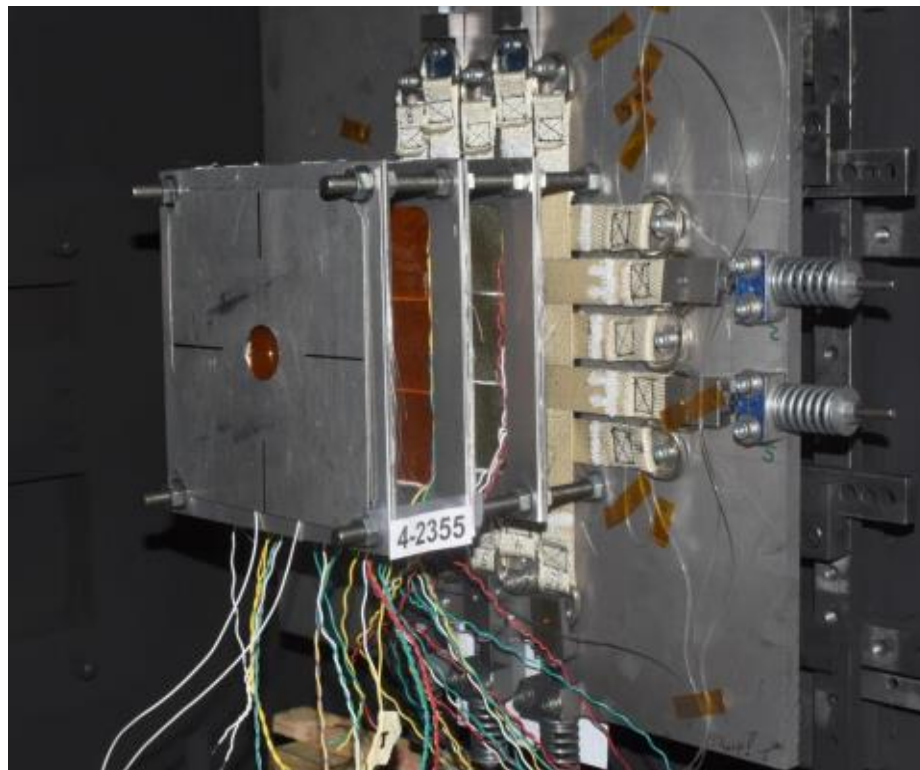


Figure 5.22 Test article before the test

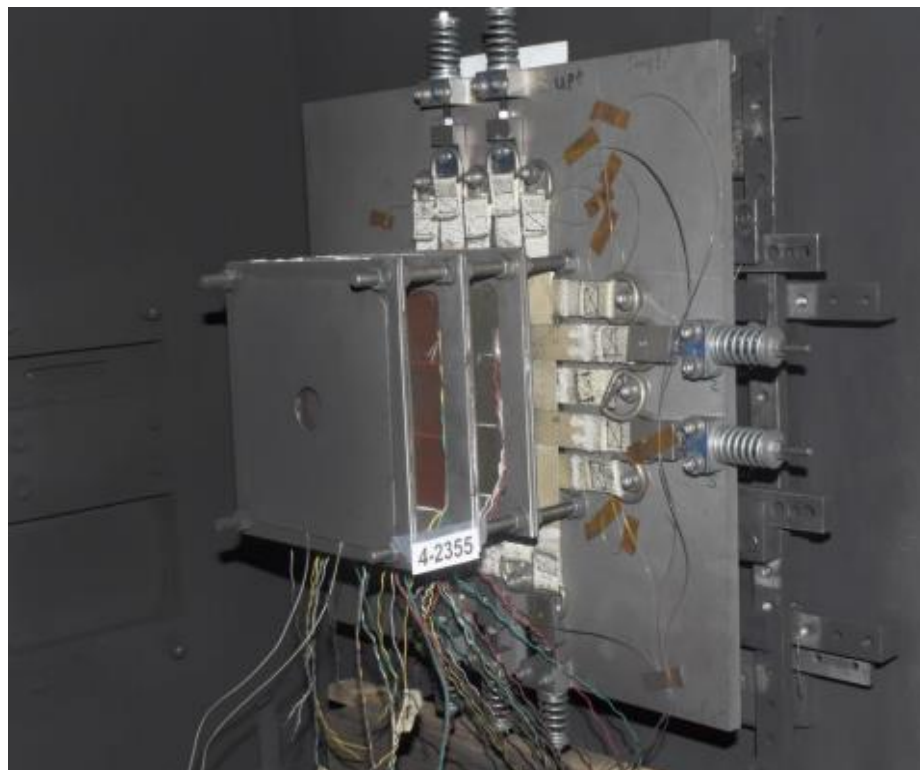


Figure 5.23 Test article after the test

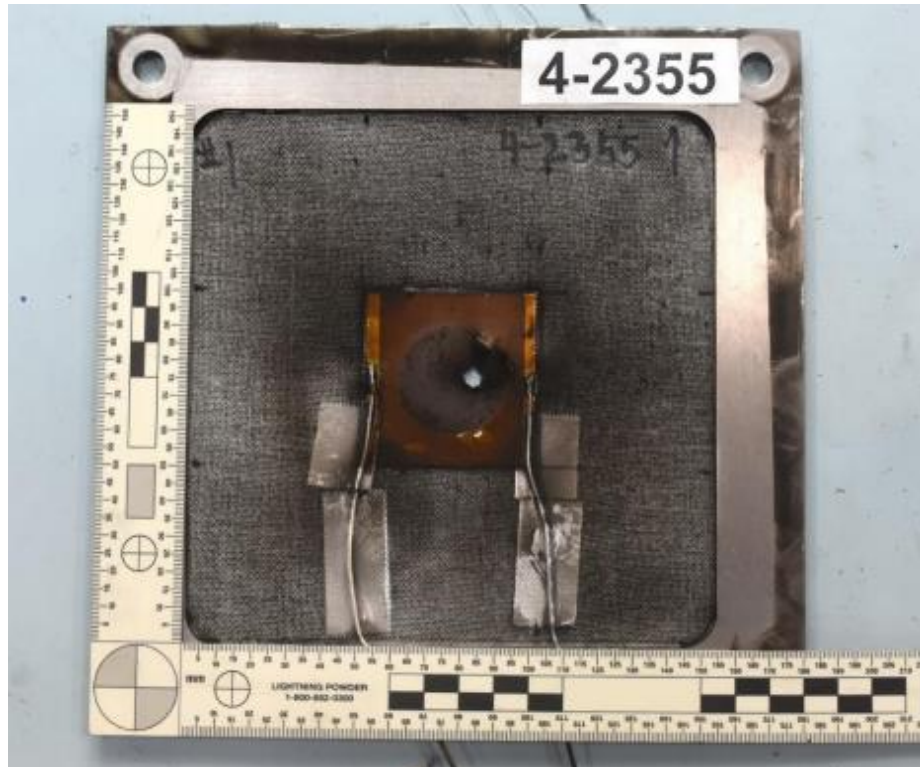


Figure 5.24 Front side of the first layer (inkjet-printed sensors) after the second test

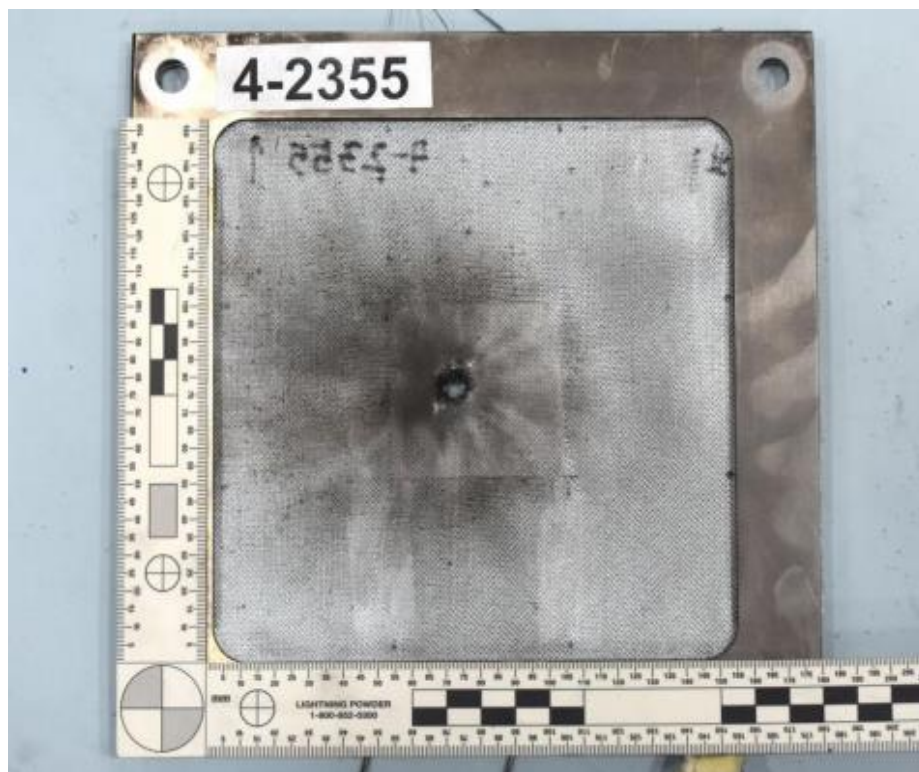


Figure 5.25 Back side of the first layer (inkjet-printed sensors) after the second test

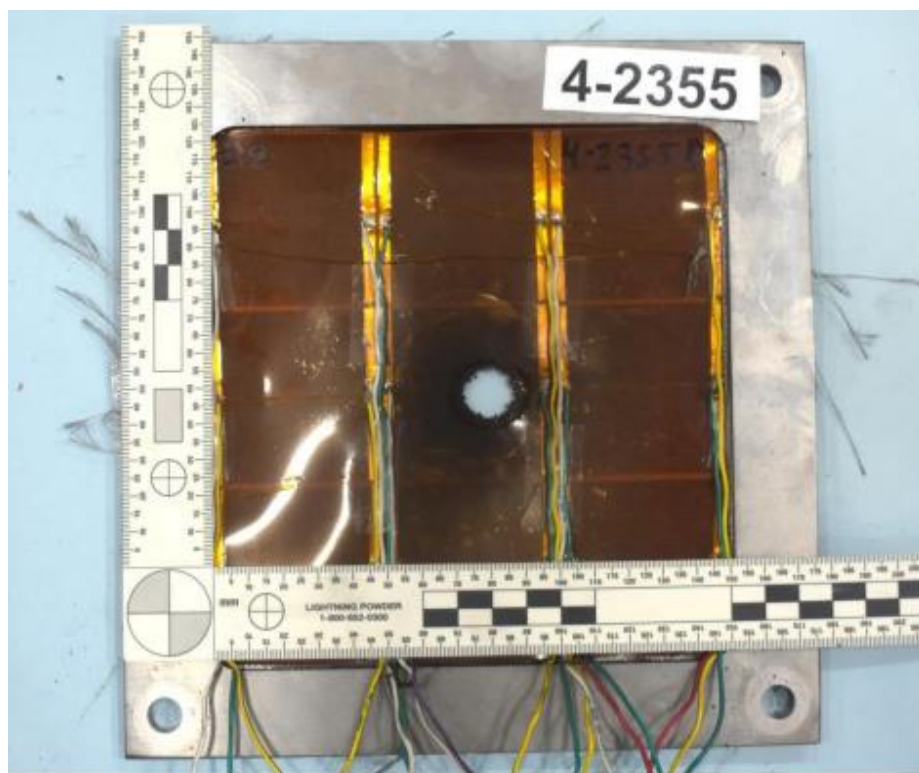


Figure 5.26 Front side of the second layer (inkjet-printed sensors) after the second test



Figure 5.27 Back side of the second layer (inkjet-printed sensors) after the second test

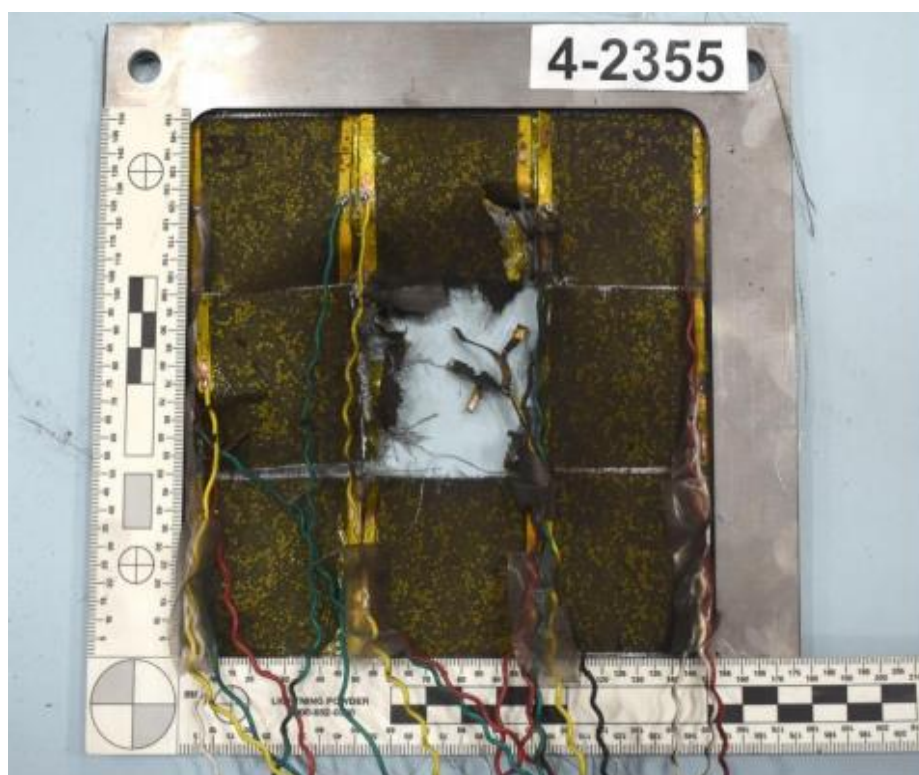


Figure 5.28 Frontside of the third layer (ink jet printed sensors) after the second test

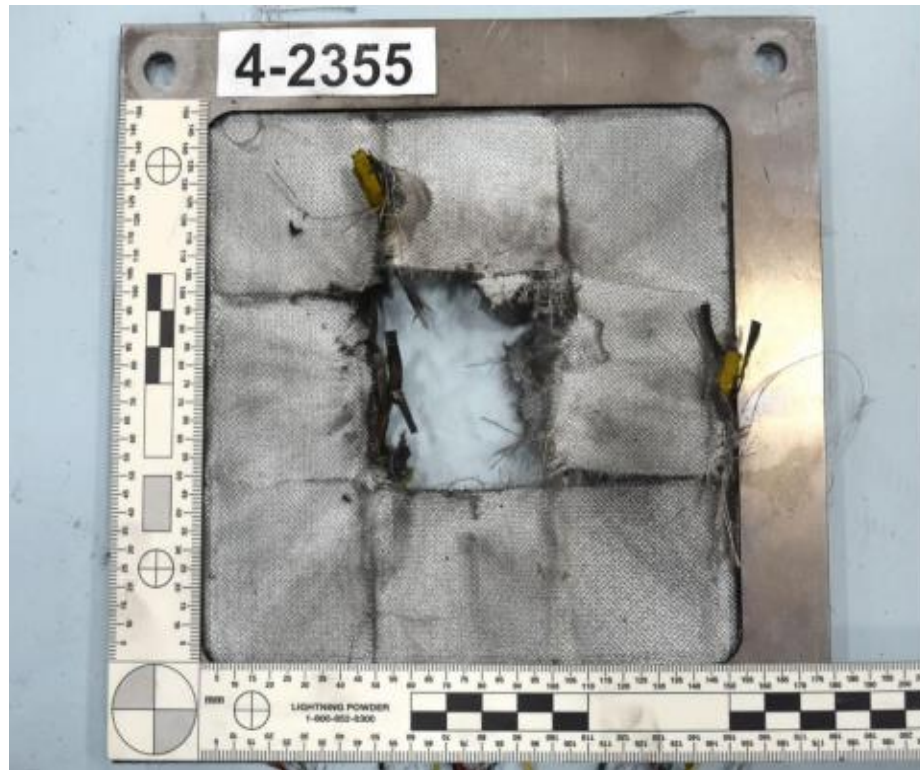


Figure 5.29 Back side of the third layer (inkjet printed sensors) after the second test

5.6. Resistance Measurement of Hybrid Sensors

As a result of the impact on the third layer consisting of 9 hybrid sensors, sensor 5, sensor 6 and their connecting wires were completely severed and the voltage shot up to 5 V, which was maximum voltage set in the data acquisition system. This can be seen in Figure A.14 and Figure A.15 in the appendix, for resistance change ratio. Sensors 2, sensor 4 and sensor 7 experienced finite resistance change which is evident from Figure A.11, Figure A.13, and Figure A.16 in the appendix respectively. The percentage change in resistance was derived for each sensor from the real-time voltage, as shown in Figure A.10 through Figure A.18 in the appendix.

Figure 5.30 shows how the damage to the test article is comparable to the strain in the form of resistive change in the plots for each sensor on the second layer of the test article.

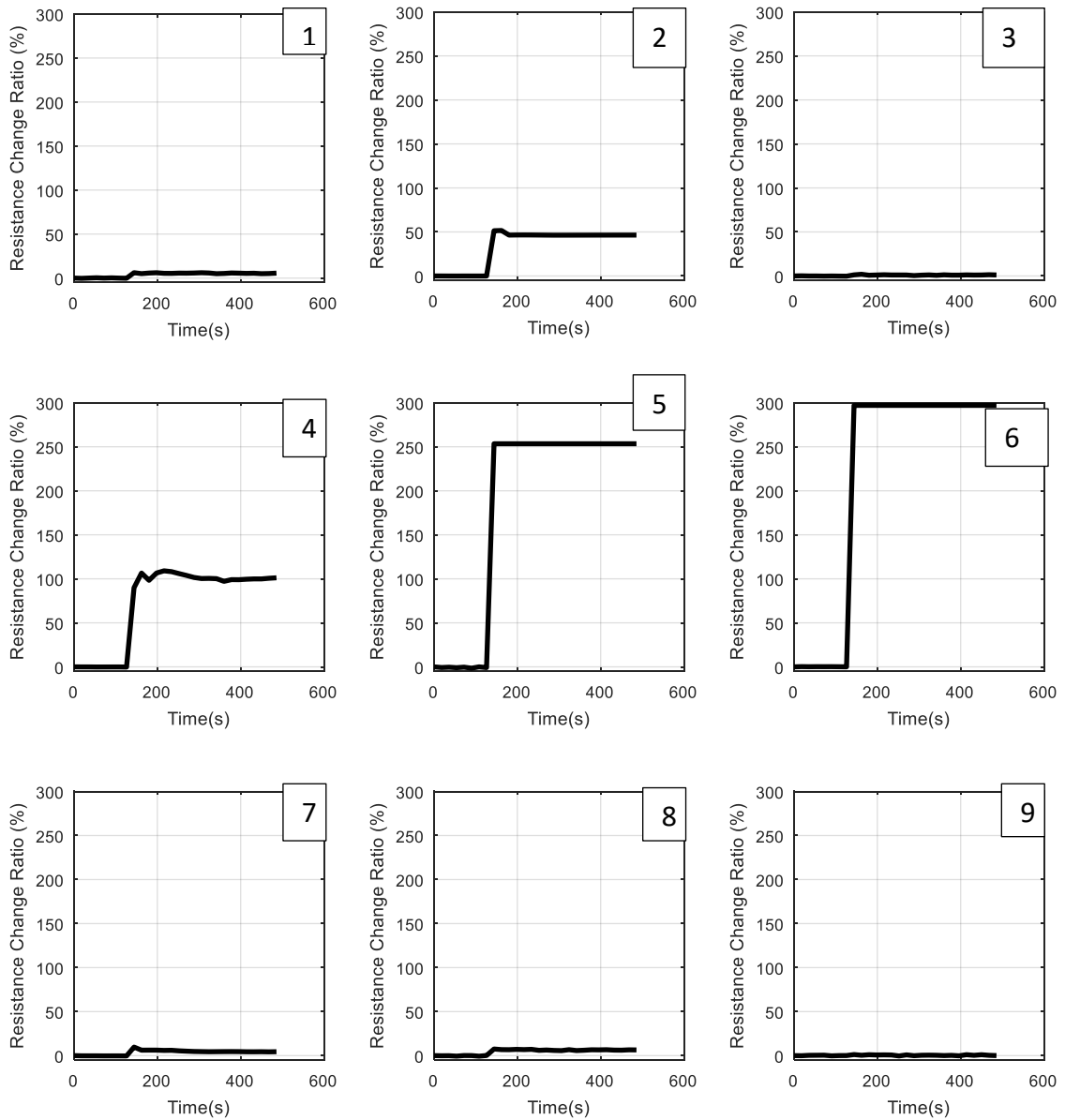


Figure 5.30 Response of different sensors during second HVIT.

5.7. Limitations of Hypervelocity Impact Test

Following limitations were recognized for the hypervelocity impact test:

- The data was acquired before and after the test only. This did not provide any information on dynamic response of the sensors.
- The velocity of the projectile was measured only before the impact. The

test provided no information on the velocity of the projectile after the impact (exit velocity) as the test chamber had no means to measure it.

- A strong shock wave was experienced by the first layer of the sensors during the first impact test which caused damage to the glass fiber and the sensor. A thin metal plate with a hole in the center was used during the second test to shield the sensors from this effect.
- Some sensors were severed during the test which resulted in loss of some data.

5.8. Discussion

Two tests were performed with two different sizes of projectiles and different sequences of hybrid sensors and inkjet-printed sensors. This provided a complete picture of the response of sensors to the projectile and to the debris cloud. Based on the impact physics and tests done in the past, it was expected that the first layer to be hit by the projectile would have a clear hole, while the following layers would sustain larger damage as they would be hit by a debris cloud. A similar pattern was observed after the HVIT at UDRI. All three layers were hit in both tests. The first layer had a clear hole of 4.5 mm diameter, while the second layer had damage of 19.2 mm diameter. The voltage readings captured by the DAQ during the test were converted to change in resistance. 23% change in resistance ratio was seen for the first layer (4.5mm diameter hole). 150% change was seen in the second layer (19.2 mm diameter hole), and in case of the third layer, the sensor in the middle was completely severed. The location and depth of damage could be detected by observing the response of the sensor number on each layer according to the nomenclature. The response could be seen in real time using the DAQ.

This shows the great potential of the sensors along with the DAQ and the control circuits to detect the damage, its location and depth of penetration by a 3mm diameter projectile at 7km/s. A structural health monitoring system can hence be developed using the hybrid CNT-GNP nanocomposite sensors.

Brandon et al., 2011 explained the working and impact testing of capacitive sensors developed for detection of impact damage by MMOD in inflatable space structures. The results showed that for similar size of projectile (3mm) shot at 7km/s, the first layer of sensors got severed with a hole of 6mm diameter, whereas, the hybrid CNT GNP sensors, (first layer) showed a resistance change ratio of 23.5% for a hole of 4.66 mm in same test conditions. For the second layer, both types of sensors had a hole of approximately 20 mm. However, the capacitance change ratio in capacitive sensors was only 10%, whereas the hybrid CNT GNP sensors underwent 150% resistance change ratio. A comparison of the two types of sensors is shown in Table 5.2. Hence, the hybrid CNT GNP sensors exhibit robustness and higher sensitivity to impact damage compared to the capacitive sensors. In addition, they are flexible, easy to develop and the electronics and data acquisition involved are simpler and cheaper. Macro-Fiber Composite (MFC) piezoelectric device is another type of sensor that has been tested for detecting and assessing MMOD strike damage on inflatable rigidizeable composite space structures (Tarazaga, Peairs, Wilkie, & Inman, 2006). The results showed that these sensors can detect damage as small as 0.79 mm. However, due to power limitations of monitoring devices, high cost of data storage and transmission, it cannot be used in large systems.

Acoustic emission sensors can detect damage in micron size scale but give an

approximate location of the damage and would require very effective noise control (Iliescu, Lakis, & Abou–Antoun, 2014). Fabric sensors made from spray-coated, piezoresistive, CNT latex thin films as sensing elements shows promising results in detection of pressure changes, and are low-cost, flexible, lightweight, robust and easy to fabricate (Wang, Gupta, Loh, & Koo, 2016). However, they have not been tested for impacts by projectile traveling at hypervelocity.

Table 5.2

Comparison of Sensitivity of Capacitive Sensors and Hybrid Nanocomposite Sensors to Impact Damage at 7 km/s for a Projectile of 3mm Diameter.

Sensor	Location on Test Article	Size of Damage	Capacitance or Resistance Change Ratio
Capacitive Copper-Polyimide sensors (Brandon, et al., 2011)	First layer	6 mm	Shorted
	Second layer	22-25 mm	10%
Piezoresistive hybrid nanocomposite sensors (Current Study)	First layer	4.66 mm	23.5%
	Second layer	20.2 mm	150%

It was observed that the FEA results from the baseline model could not capture the right mode of damage for second, third and fourth layers. The HVIT results show that the first layer sustains a clear hole, while the following layers had bigger damage size. This is because the first layer is impacted by the projectile, but the following layers are impacted by a debris cloud consisting of shattered projectile and debris from the previous layer. However, in the finite element model, the projectile is assumed to be rigid. This resulted in similar damage for all the layers during the simulation. Moreover, the material

models used for the finite element model did not represent the actual materials which led to the discrepancies between the experimental results and the simulation results.

6. Conclusions and Future Work

6.1. Conclusions

Hybrid CNT-GNP nanocomposites were developed using a novel technique using a laser marker to cut the GNP and distribute them in a pattern in the matrix. The effect of distributing GNPs in a uniform fashion and aspect ratio of GNPs on piezoresistivity and electrical conductivity was studied

The hybrid nanocomposite sensors were tested for their electrical response to holes added with a drill. A test fixture was successfully designed and manufactured for the HVIT that simulated the layers of fabric of inflatable space structures. DAQ system and power system were successfully designed and tested to be used along with the nanocomposite sensors to form a health monitoring system that can be integrated with space inflatable structures. The process to simulate the HVIT was recognized and executed to obtain a baseline model. However, the test could not be simulated due to unavailability of material properties. The HVIT was successfully carried out and proved that the hybrid nanocomposite sensors can detect damage due to MMOD in space inflatable structures efficiently.

The primary scientific conclusions of this research are:

- 1) Using laser marker to develop the hybrid CNT-GNP/epoxy nanocomposites resulted in better controlled microstructure of the hybrid nanocomposites.
- 2) The percolation based numerical model (Gbaguidi, Namilae, & Kim, 2017) showed that distribution of graphite platelets in a uniform fashion and aspect ratio of the graphite platelets resulted in an enhanced piezoresistive behavior at nanoscale. However, during tests with 1 mm diameter graphite platelets, it was

observed that distribution and aspect ratio of the platelets have no effect on piezoresistivity of the nanocomposites. This could be due to different tunneling mechanisms at micro-size and macro-size level.

- 3) Change in resistance ratio due to a 4.5 mm diameter hole added statically was found to be 2%, whereas it was 23.5% when damage of same size was sustained by the sensors during the HVIT. Hence, the sensors went through 10 times higher change in resistance for impacts at high strain rates and their response is strain rate dependent. This could be due to dynamic strain and temperature effects along with piezoresistivity of the sensors.
- 4) The HVIT was successfully carried out and proved that the hybrid nanocomposite sensors could detect damage due to MMOD of 3mm diameter (at 7km/s), its location and penetration depth in space inflatable structures efficiently.
- 5) The hybrid GNP-CNT/epoxy nanocomposite piezoresistive sensors were found to be more robust and provided better resolution to impact damage caused by a projectile of 3mm at 7 km/s as compared to capacitive sensors that have been tested for the same technology in past (Brandon, et al., 2011).
- 6) The hybrid GNP-CNT/epoxy nanocomposites were also found to be power efficient and economic compared to MFC composite piezoelectric sensors, and more accurate in determination of damage and its location as compared to sensors based on acoustic emission technology.

In summary the hybrid CNT-GNP/epoxy nanocomposites are effective in detecting MMOD impact damage in space inflatable structures.

6.2. Future Work

Following are the recommendations for future work:

- 1) The technique followed to cut GNP in laser marker can be used to study the effect of size, shape and weight% of GNP on the hybrid nanocomposites. It was found that aspect ratio and distribution of GNPs did not cause any effect on piezoresistivity of the nanocomposites. Further investigation is required to determine other factors playing a role in this behavior like contact between CNT and GNP.
- 2) In order to validate the experimental results regarding no effect of aspect ratio and distribution of graphite platelets on piezoresistivity, comparison should be drawn with numerical work done for larger size of graphite platelets.
- 3) A hypervelocity Impact simulation was attempted in LS Dyna. However, it was realized that the simulation required material characterization tests that could not be carried out due to limited resources. These can be carried out at other facilities that provide high strain tensile testing. It is recommended that MAT_058 from LS Dyna material library is used for this simulation. Once the mechanical properties are known, characterization tests can be carried out in LS Dyna to verify the material model. Results achieved from the HVIT discussed in this work can be compared and the finite element model can be validated. Once this has been achieved, this model can be used in the future to predict the impact mechanics when parameters like stand-off distance between the layers, thickness of the layers are changed.
- 4) During the HVIT, sensors of 2 inch by 2 inch were used, which showed excellent

response to the damage. However, in order to apply blanket technology to large inflatable structures, tests must be done on larger sizes of sensors so that the system is power efficient and economic.

- 5) The electronic circuit and the data acquisition system used during the HVIT captured the change in voltage in a periodic manner. Every sensor was scanned for 2 seconds one after another. This gave a clear picture of the sensors' response before and after impact. However, with continuous power to each sensor, its instantaneous response during the impact can also be captured.

REFERENCES

- Advanced Exploration Systems. (2017, November 16). Retrieved from NASA:
<https://www.nasa.gov/content/bigelow-expandable-activity-module>
- Ajayan, P. M., Schadler, L. S., Giannaris, C., & Rubio. (2000). A Single-walled carbon nanotube–polymer composites: Strength and weakness. *Advanced Material* 12, 750–753.
- Al-Saleh, M. H. (2015). Electrical and mechanical properties of graphene/carbon nanotube hybrid nanocomposites. *Synthetic Metals*, 209, 41-46.
- Anees M. (2017). *Development and Characterization of Piezoresistive Nanocomposites for Sensing applications*. Daytona Beach.
- Arnold, J., Christiansen, E., Davis, A., Hyde, J., Lear, D., Liou, J., . . . Ryan, S. (2009). Handbook for Designing MMOD Protection.
- Bae, S. H., Lee, Y., Sharma, B. K., Lee, H. J., Kim, J. H., & Ahn, J. H. (2013). Graphene-based transparent strain sensor. *Carbon*, 51, 236-242.
- Balazs, A. C., Emrick, T., & Russell, T. P. (2006). Nanoparticle polymer composites: where two small worlds meet. *Science*, 314 (5802), 1107-1110.
- Bhattacharya, M. (2016). Polymer nanocomposites—a comparison between carbon nanotubes, graphene, and clay as nanofillers. *Materials*, 9(4), 262.
- Bonavolontà, C., Camerlingo, C., Carotenuto, G., De Nicola, S., Longo, A., Meola, C., & Valentino, M. (2016). Characterization of piezoresistive properties of graphene-supported polymer coating for strain sensor applications. *Sensors and Actuators A: Physical*, 252, 26-34.
- Brandon, E. J., Vozoff, M., Kolawa, E. A., Studor, G. F., Lyons, F., Keller, M. W., . . . Banks, D. L. (2011). Structural health management technologies for inflatable/deployable structures: Integrating sensing and self-healing. *Acta Astronautica*, 68(7-8), 883-903.
- Carney, K., Melis, M., Fasanella, E. L., Lyle, K. H., & Gabrys, J. (2004). Material

modeling of space shuttle leading edge and external tank materials for use in the Columbia accident investigation.

- Chatterjee, S., Nafezarefi, F., Tai, N. H., Schlagenhaut, L., Nüesch, F. A., & Chu, B. T. (2012). Size and synergy effects of nanofiller hybrids including graphene nanoplatelets and carbon nanotubes in mechanical properties of epoxy composites. *Carbon*, *50*(15), 5380-5386.
- Cho, D., Lee, S., Yang, G. M., Fukushima, H., & Drzal, L. T. (2005). Dynamic mechanical and thermal properties of phenylethynyl-terminated polyimide composites reinforced with expanded graphite nanoplatelets. *Macromolecular Materials and Engineering Volume 290*, 179–187.
- Christiansen, E. L., Nagy, K., Lear, D. M., & Prior, T. G. (2009). Space station MMOD shielding. *Acta Astronautica*, *65* (7-8), 921-929.
- Das, T. K., & Prusty, S. (2013). Graphene-based polymer composites and their applications. *Polymer-Plastics Technology and Engineering*, *52*(4), 319-331.
- Dharap, P., Li, Z., Nagarajaiah, S., & Barrera, E. V. (2004). Nanotube film based on single-wall carbon nanotubes for strain sensing. *Nanotechnology*, *15*(3), 379.
- Fan, L. W., Fang, X., Wang, X., Zeng, Y., Xiao, Y. Q., Yu, Z. T., & Cen, K. F. (2013). Effects of various carbon nanofillers on the thermal conductivity and energy storage properties of paraffin-based nanocomposite phase change materials. *Applied Energy*, *110*, 163-172.
- Fiedler, B., Gojny, F. H., Wichmann, M. H., Nolte, M. C., & Schulte, K. (2006). Fundamental aspects of nano-reinforced composites. *Composites science and technology*, *66*(16), 3115-3125.
- Gbaguidi, A., Namilae, S., & Kim, D. (2017). Monte Carlo Model for Piezoresistivity of Hybrid Nanocomposites. *ASME Journal of Engineering Materials and Technology*, 11.
- Geim, A. K. (2009). Graphene: status and prospects. *Science*, *324*(5934), 1530-1534.
- Genesis I*. (2019, March 1). Retrieved from Wikipedia:
https://en.wikipedia.org/wiki/Genesis_I

- Genesis II*. (2018, July 25). Retrieved from Wikipedia:
https://en.wikipedia.org/wiki/Genesis_II
- Gómez-Navarro, C. W., & Kern, K. (2007). Electronic transport properties of individual chemically reduced graphene oxide sheets. *Nano letters*, *7*(11), 3499-3503.
- Häuplik-Meusburger, S., Sommer, B., & Aguzzi, M. (2009). Inflatable technologies: adaptability from dream to reality. *Acta Astronautica*, *65* (5-6), 841-852.
- Hu, N., Fukunaga, H., Atobe, S., Liu, Y., & Li, J. (2011). Piezoresistive strain sensors made from carbon nanotubes based polymer nanocomposites. *Sensors*, *11*(11), 10691-10723.
- Hwang, S. H., Park, H. W., & Park, Y.-B. (2013). Piezoresistive behavior and multidirectional strain sensing ability of carbon nanotube–graphene nanoplatelet hybrid sheets. *Smart Materials and Structures*, *22*(1), 15013.
- Iliescu, L. E., Lakis, A. A., & Abou–Antoun, A. (2014). Hypervelocity Impact (HVI) Tests & Signal Recordings. *Universal Journal of Aeronautical & Aerospace Sciences*, *2*, 80-113.
- Jackson, K. E., Fasanella, E. L., & Littell, J. D. (2017). Development of a Continuum Damage Mechanics Material Model of a Graphite Kevlar Hybrid Fabric for Simulating the Impact Response of Energy Absorbing Kevlar Hybrid Fabric for Simulating the Impact Response of Energy absorbing.
- Jang, B. Z., & Zhamu, A. (2008). Processing of nanographene platelets (NGPs) and NGP nanocomposites: a review. *Journal of Materials Science*, *43* (15), 5092-5101.
- Kang, I., Schulz, M. J., Kim, J. H., Shanov, V., & Shi, D. (2006). A carbon nanotube strain sensor for structural health monitoring. *Smart materials and structures*, *15* (3), 737.
- Keller, T. (2011). Recent all-composite and hybrid fiber reinforced polymer bridges and buildings. *Progress in Structural Engineering and Materials*, *3*, 132–140.
- Kennedy, K. J., Raboin, J., Spexarth, G., & Valle, G. (2000). Inflatable Structures Technology Handbook. Chapter 21.

- Kuilla, T., Bhadra, S., Yao, D., Kim, N. H., Bose, S., & Lee, J. H. (2010). Recent advances in graphene based polymer composites. *Progress in Polymer Science* 35 (11), 1350-1375.
- Lee, C., Jug, L., & Meng, E. (2013). High strain biocompatible polydimethylsiloxane-based conductive graphene and multiwalled carbon nanotube nanocomposite strain sensors. *Applied Physics Letters*, 102(18), 183511.
- Lemmens, S., Krag, H., Rosebrock, J., & Carnelli, I. (2013). Radar mappings for attitude analysis of objects in orbit. *6th European Conference on Space Debris Vol. 723*, (p. 20).
- Li, J., & Namilae, S. (2016). Nanotube Sheet — Graphite Hybrid Nanocomposite for Damage Detection. *The Minerals, Metals & Materials Society (eds) TMS 2016 145th Annual Meeting & Exhibition*. Springer, Cham.
- Li, J., Wong, P. S., & Kim, J. K. (2008). Hybrid nanocomposites containing carbon nanotubes and graphite nanoplatelets. *Materials Science and Engineering: A*, 483, 660-663.
- Li, W., Dichiara, A., & Bai, J. (2013). Carbon nanotube–graphene nanoplatelet hybrids as high-performance multifunctional reinforcements in epoxy composites. *Composites Science and Technology*, 74, 221-227.
- Li, Y., Wang, K., Wei, J., Gu, Z., Wang, Z., & Luo, J. (2005). Tensile properties of long aligned double-walled carbon nanotube strands. *Carbon*, 43, 31-35.
- Lim, C. T., Shim, V. P., & Ng, Y. H. (2003). Finite-element modeling of the ballistic impact of fabric armor. *International Journal of Impact Engineering*, , 28(1), 13-31.
- Litteken, D. A. (2017). Strain Monitoring of Flexible Structures.
- Luo, S., & Liu, T. (2013). SWCNT/graphite nanoplatelet hybrid thin films for selftemperature- compensated, highly sensitive, and extensible piezoresistive sensors. *Advanced Materials*, 25 (39), 5650–5657.
- Ma, P. C., Siddiqui, N. A., Marom, G., & Kim, J. K. (2010). Dispersion and functionalization of carbon nanotubes for polymer-based nanocomposites: a

review. *Composites Part A: Applied Science and Manufacturing*, 41 (10), 1345-1367.

Matweb.com. (2015, August 29). Retrieved from Matweb-The Online Materials Information Resource:
<http://www.matweb.com/search/DataSheet.aspx?MatGUID=4f19a42be94546b686bbf43f79c51b7d>

Moniruzzaman, M., & Winey, K. I. (2006). Polymer nanocomposites containing carbon nanotubes. *Macromolecules*, 39(16), 5194-5205.

Mukhopadhyay, P., & Gupta, R. K. (2011). Trends and frontiers in graphene-based polymer nanocomposites. *Plastics engineering*, 67 (1), 32-42.

Namilae, S., Li, J., & Chava, S. (2018). Improved piezoresistivity and damage detection application of hybrid carbon nanotube sheet-graphite platelet nanocomposites. *Mechanics of Advanced Materials and Structure*, 1-15.

Nilakantan, G., Keefe, M., Bogetti, T. A., & Gillespie Jr, J. W. (2010). Multiscale modeling of the impact of textile fabrics based on hybrid element analysis. *International Journal of Impact Engineering*, 37(10), 1056-1071.

Njuguna, J., & Pielichowski, K. (2003). Polymer nanocomposites for aerospace applications: properties. *Advanced Engineering Materials*, 769-778.

Obitayo, W., & Liu, T. (2012). A Review: Carbon Nanotube-Based Piezoresistive Strain Sensors. *Journal of Sensors*, 12.

Park, E. J., Kim, K. J., Park, D. W., & Shim, S. E. (2011). Colloidal Heterocoagulation for Preparation of Multi-Walled Carbon Nanotube/PMMA Nanocomposite Started with Bulk Resin. *Journal of Dispersion Science and Technology*, 32(11), 1574–1581.

Ramanathan, T. (2007). Graphitic nanofillers in PMMA nanocomposites—an investigation of particle size and dispersion and their influence on nanocomposite properties. *J. Polym. Sci. B: Polym. Phys.* 45, 2097–2112.

Ramanathan, T., Abdala, A. A., Stankovich, S., Dikin, D. A., Herrera-Alonso, M., Piner, R. D., & Nguyen, S. T. (2008). Functionalized graphene sheets for polymer

nanocomposites. *Nature nanotechnology*, 3 (6), 327.

Ramanathan, T., Abdala, A. A., Stankovich, S., Dikin, D. A., Herrera-Alonso, M., Piner, R. D., . . . Brinson, L. C. (2008). Functionalized graphene sheets for polymer nanocomposites. *Nature nanotechnology*, 3(6), 327.

Ramanathan, T., Liu, H., & Brinson, L. C. (2005). Functionalized SWNT polymer nanocomposites for dramatic property improvement. *Polymer Science. B : Polymer Physics* 43, 2269 –2279.

Ray, S. S., & Okamoto. (2003). M. Polymer/layered silicate nanocomposites: a review from preparation to processing. *Progress in Polymer Science* 28, 1539 –1641.

Sagalianov, I., Vovchenko, L., Matzui, L., & Lazarenko, O. (2017). Synergistic enhancement of the percolation threshold in hybrid polymeric nanocomposites based on carbon nanotubes and graphite nanoplatelets. *Nanoscale research letters*, 12 (1), 140.

Sandler, J. K., Kirk, J. E., Kinloch, I. A., Shaffer, M. S., & Windle, A. H. (2003). Ultra-low electrical percolation threshold in carbon-nanotube-epoxy composites. *Polymer*, 44 (19), 5893-5899.

Shahkarami, A., & Vaziri, R. (2007). A continuum shell finite element model for impact simulation of woven fabrics. *International Journal of Impact Engineering*, 104-119.

Space Debris. (2018, November 1). Retrieved from ESA:
https://www.esa.int/Our_Activities/Operations/Space_Safety_Security/Space_Debris/Hypervelocity_impacts_and_protecting_spacecraft

Stankovich, S., Dikin, D. A., Dommett, G. H., Kohlhaas, K. M., Zimney, E. J., Stach, E. A., . . . Ruoff, R. S. (2006). Graphene Based Composite Materials. *Nature*, 282-286.

Tarazaga, P. A., Peairs, D. M., Wilkie, W. K., & Inman, D. J. (2006). Structural health monitoring of an inflatable boom subjected to simulated micrometeoroid/orbital debris damage. *Nondestructive Evaluation and Health Monitoring of Aerospace Materials, Composites, and Civil Infrastructure Vol. 6176* (p. 61760N). San Diego: International Society for Optics and Photonics.

- Thostenson, E. T., Ren, Z., & Chou, T. W. (2001). Advances in the science and technology of carbon nanotubes and their composites: a review. *Composites Science and Technology* 61, 1899–1912.
- Usuki, A., Hasegawa, N., & Kato. (2005). M. Polymer– clay nanocomposites. *Advanced Polymer Science* 179, 135 –195.
- Wang, L., Gupta, S., Loh, K. J., & Koo, H. S. (2016). NanoComposite Fabric Sensors for Monitoring Inflatable and Deployable Space Structures. *ASME 2016 Conference on Smart Materials, Adaptive Structures and Intelligent Systems* (pp. V001T05A006-V001T05A006). American Society of Mechanical Engineers.
- Yen, C. F. (2002). Ballistic impact modeling of composite materials. *Proceedings of the 7th international LS-DYNA users conference Volume 6*, (pp. 15-23).
- Yu, A., Ramesh, P., Sun, X., Bekyarova, E., Itkis, M. E., & Haddon, R. C. (2008). Enhanced thermal conductivity in a hybrid graphite nanoplatelet–carbon nanotube filler for epoxy composites. *Advanced Materials*, 20 (24), 4740-4744.
- Yue, L., Pircheraghi, G., Monemian, S. A., & Manas-Zloczower, I. (2014). Epoxy composites with carbon nanotubes and graphene nanoplatelets–Dispersion and synergy effects. *Carbon*, 78, 268-278.
- Zhao, Q., Nardelli, M. B., & Bernholc, J. (2002). Ultimate strength of carbon nanotubes: A theoretical study. *Physical Review B*, 65 (14), 144105.
- Zheng, W., & Wong, S. C. (2003). Electrical conductivity and dielectric properties of PMMA/expanded graphite composites. *Computer Science Technology* 63, 225 – 235.
- Zheng, W., Lu, X. H., & Wong, S. C. (2004). Electrical and mechanical properties of expanded graphite reinforced high-density polyethylene. *Applied Polymer Science* 91, 2781–2788.

A. APPENDIX

The following plots show the piezoresistive response of the sensors before and after the two hyper velocity impact tests. It is observed that the sensors that were not impacted by the projectile, also experience some strain before and after the test. It is speculated that one of the sources of this effect could be the process of creating vacuum inside the chamber after the DAQ system was turned on. Other sources of dynamic strain could be the shock wave during the impact, bending of the glass fiber fabric (carrying the sensors), and temperature and pressure changes in the chamber, as it was sealed and opened.

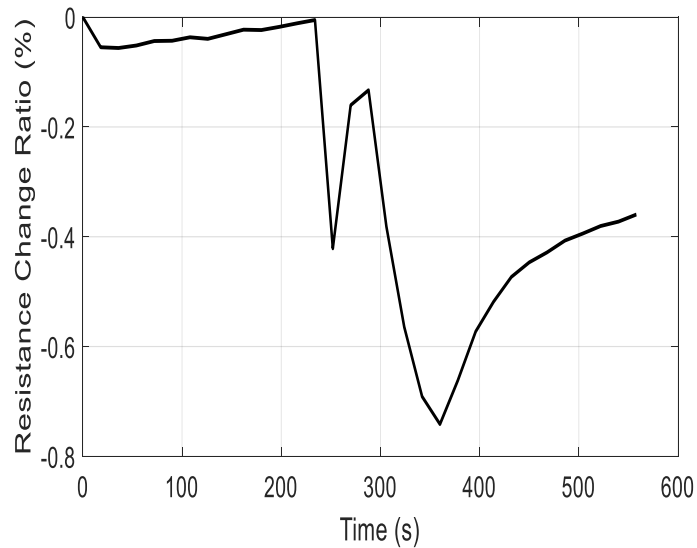


Figure A.1 Resistance change ratio for sensor 1 in the array during the first test.

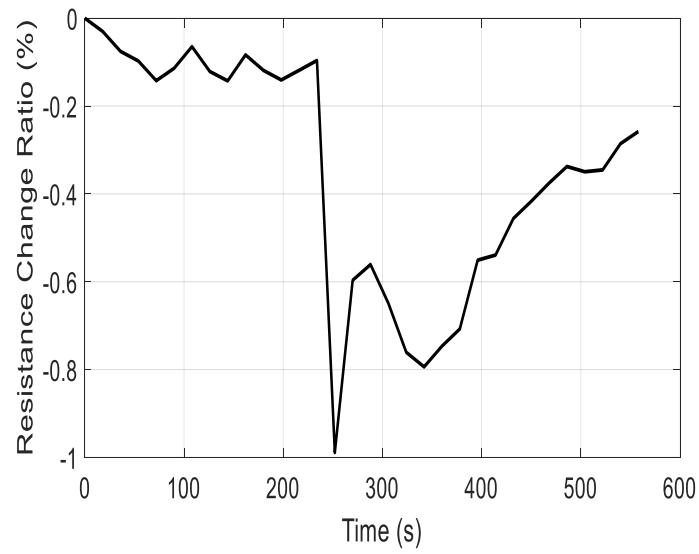


Figure A.2 Resistance change ratio for sensor 2 in the array during the first test

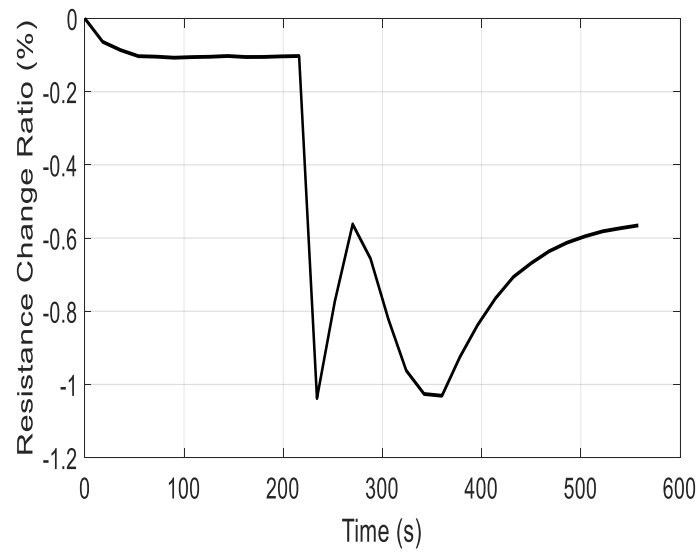


Figure A.3 Resistance change ratio for sensor 3 in the array during the first test

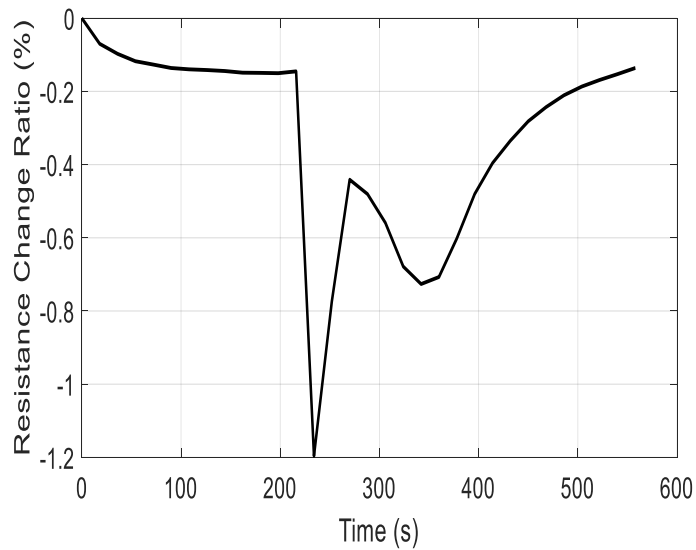


Figure A.4 Resistance change ratio for sensor 4 in the array during the first test

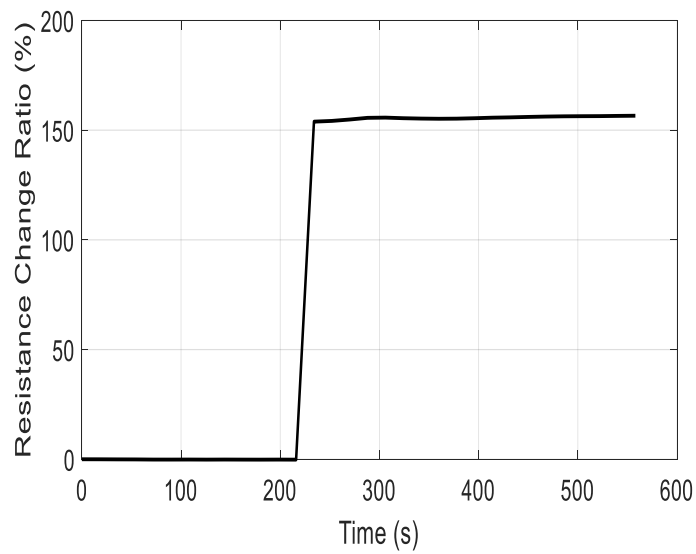


Figure A.5 Resistance change ratio for sensor 5 in the array during the first test

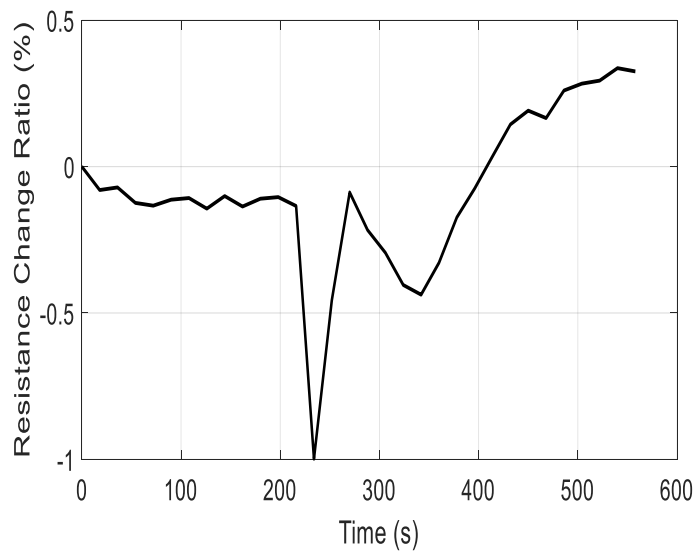


Figure A.6 Resistance change ratio for sensor 6 in the array during the first test

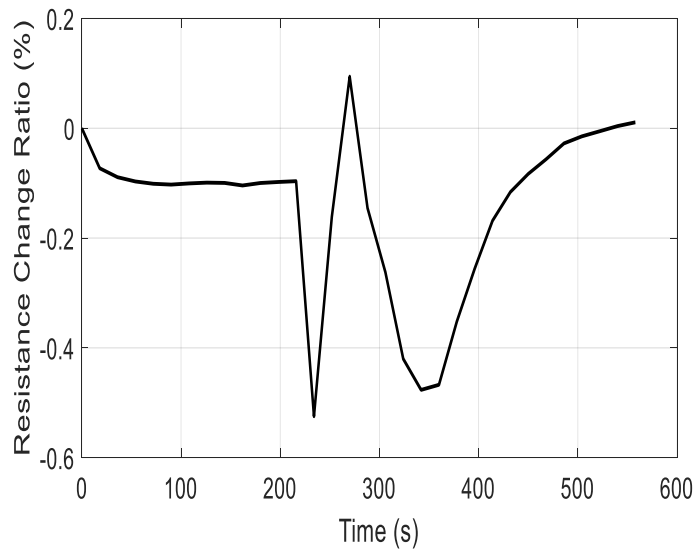


Figure A.7 Resistance change ratio for sensor 7 in the array during the first test

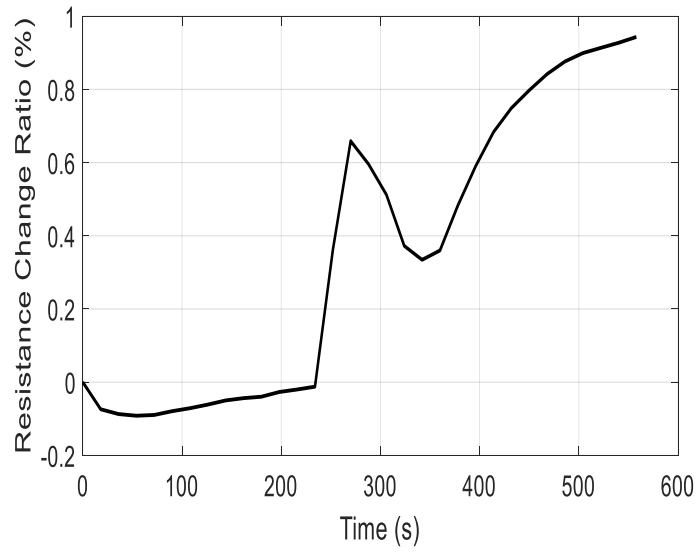


Figure A.8 Resistance change ratio for sensor 8 in the array during the first test

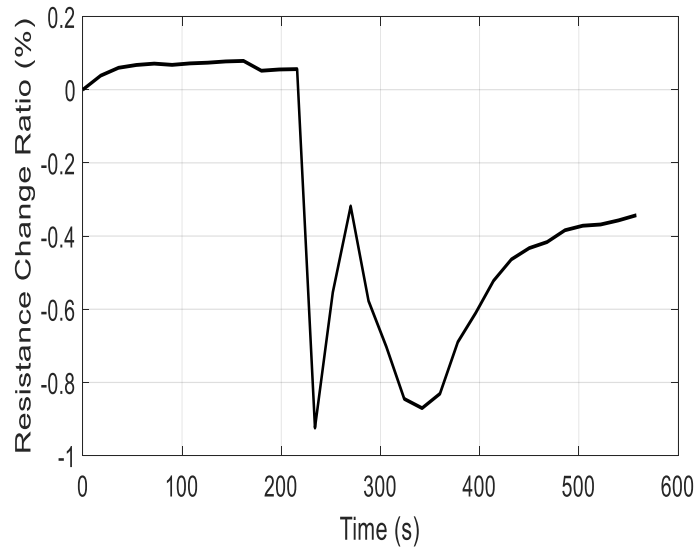


Figure A.9 Resistance change ratio for sensor 9 in the array during the first test

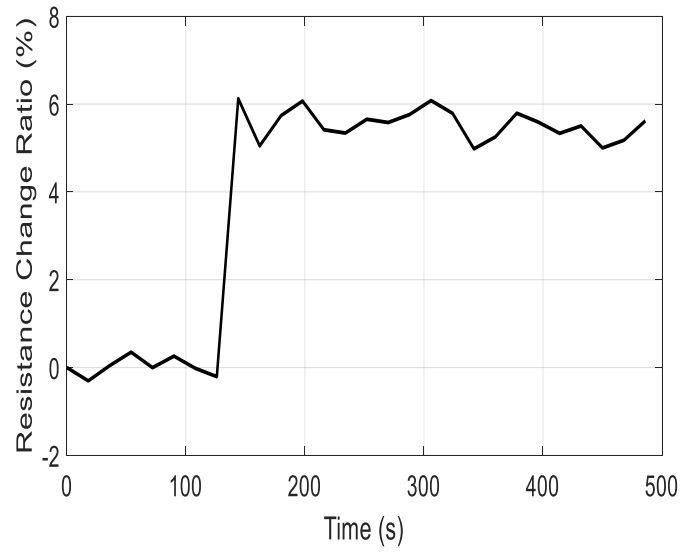


Figure A.10 Resistance change ratio for sensor 1 in the array during the second test

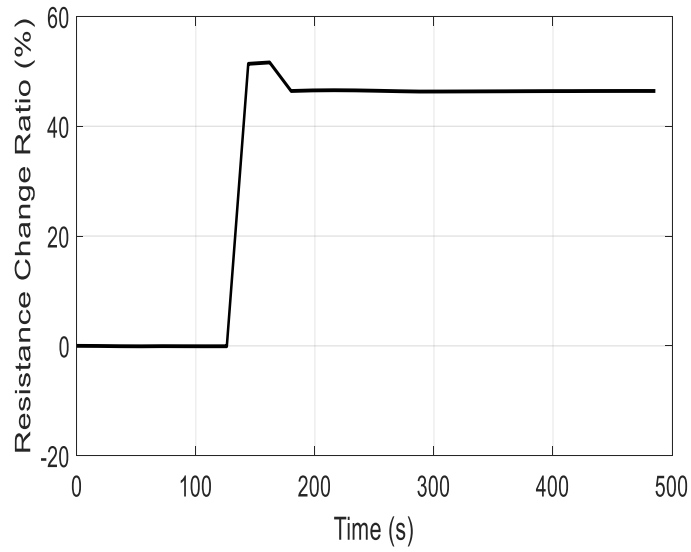


Figure A.11 Resistance change ratio for sensor 2 in the array during the second test

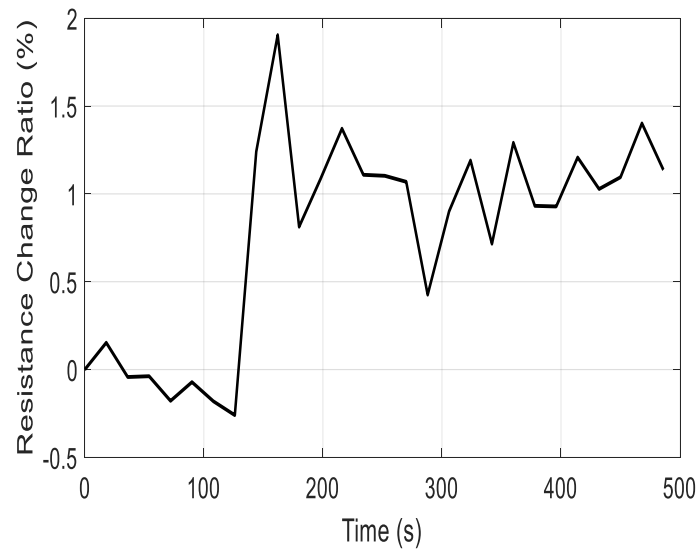


Figure A.12 Resistance change ratio for sensor 3 in the array during the second test

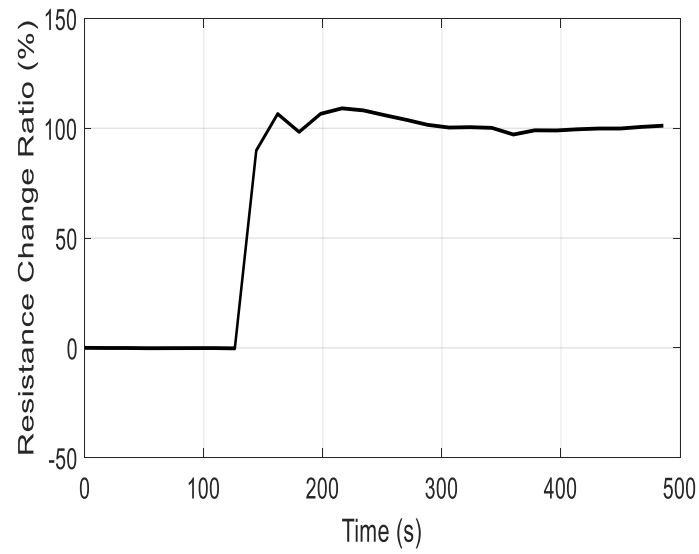


Figure A.13 Resistance change ratio for sensor 4 in the array during the second test

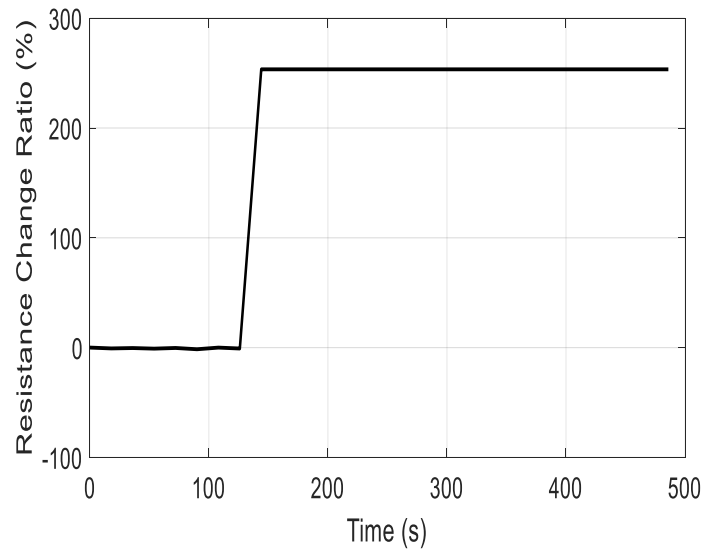


Figure A.14 Resistance change ratio for sensor 5 in the array during the second test

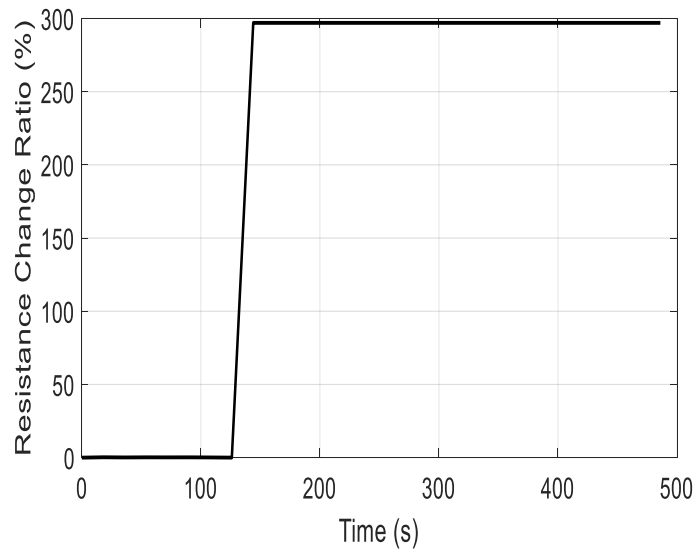


Figure A.15 Resistance change ratio for sensor 6 in the array during the second test

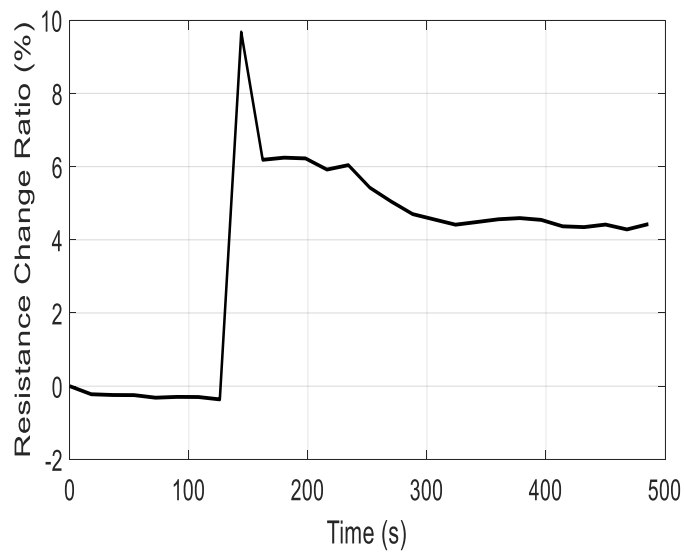


Figure A.16 Resistance change ratio for sensor 7 in the array during the second test

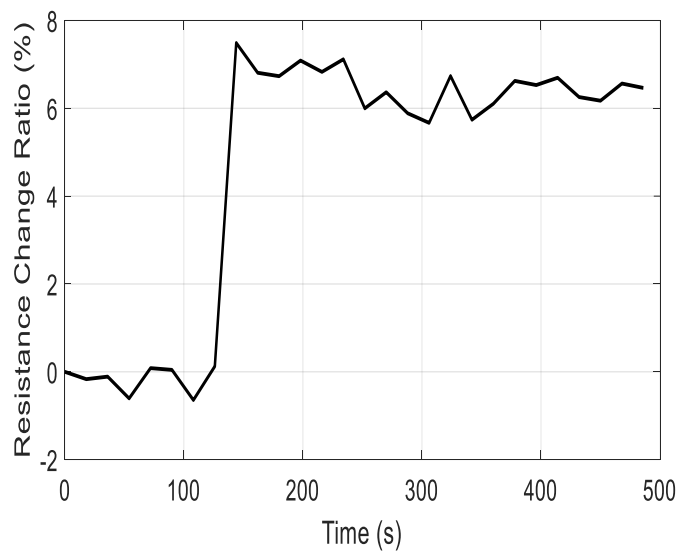


Figure A.17 Resistance change ratio for sensor 8 in the array during the second test

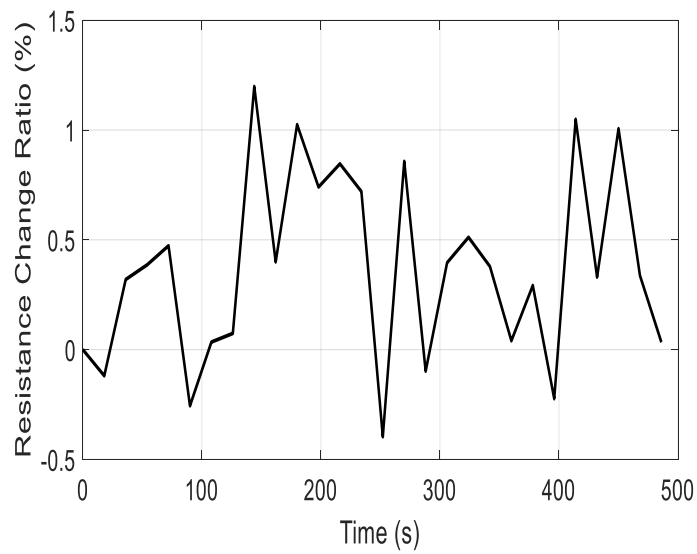


Figure A.18 Resistance change ratio for sensor 9 in the array during the second test